



**NASA  
Technical  
Paper  
3360**

September 1993

**Wind Tunnel Investigations  
of Forebody Strakes for Yaw  
Control on F/A-18 Model at  
Subsonic and Transonic Speeds**

Gary E. Erickson  
and Daniel G. Murri



**NASA  
Technical  
Paper  
3360**

1993

**Wind Tunnel Investigations  
of Forebody Strakes for Yaw  
Control on F/A-18 Model at  
Subsonic and Transonic Speeds**

Gary E. Erickson  
and Daniel G. Murri  
*Langley Research Center  
Hampton, Virginia*

## Contents

Summary . . . . .	1
Introduction . . . . .	1
Symbols . . . . .	2
Experimental Investigation . . . . .	2
Model Description and Test Apparatus . . . . .	2
Flow Visualization Techniques . . . . .	3
Wind Tunnel Facilities and Test Conditions . . . . .	4
Discussion of Results . . . . .	5
Baseline Strake Results at Subsonic and Transonic Speeds . . . . .	5
Off-surface flow visualization . . . . .	5
Surface flow visualization . . . . .	7
Longitudinal and lateral-directional characteristics . . . . .	7
Forebody surface static pressure distributions . . . . .	10
LEX upper surface static pressure distributions . . . . .	11
Strake Planform Effects . . . . .	12
Longitudinal and lateral-directional characteristics . . . . .	12
Forebody surface static pressure distributions . . . . .	13
Concluding Remarks . . . . .	13
References . . . . .	14
Figures . . . . .	16

## Summary

Wind tunnel investigations were conducted at free-stream Mach numbers of 0.20 to 0.90 with 0.06-scale models of the F/A-18 aircraft with forebody strake for high-angle-of-attack yaw control. The strake was mounted to one side of the forebody at a radial position  $120^\circ$  above the bottom centerline and was normal to the surface. This simulated an actuated conformal strake deployment yielding maximum yaw control. Test data are presented on the effects of Mach number and strake planform on the yaw control effectiveness and the character of the strake-vortex-induced flow field at high angles of attack.

Results from this study show that the strake produces large yaw control increments at high angles of attack that exceed the effect of conventional rudders at low angles of attack. The strake yaw control effectiveness diminishes with increasing Mach number but continues to exceed the effect of rudder deflection at angles of attack greater than  $30^\circ$ . The character of the vortex-dominated flow field is similar at subsonic and transonic speeds. The strake vortex core does not directly interact with the model flow field at angles of attack above approximately  $25^\circ$ . However, the strake vortex induces a circulation of opposite sense about the forebody. The induced effect of the strake vortex is manifested on the strake-off side of the forebody by an acceleration of the attached flow along the surface, a delay in boundary-layer separation, and a stronger forebody primary vortex. The differential suction pressures induced on the forebody, acting through the long forebody moment arm, produce large yawing moments at high angles of attack. The primary vortex shed from the strake-off side of the forebody is coupled to the wing leading-edge extension (LEX) vortex flow. The forebody vortex becomes decoupled and subsequently breaks down when the separated flow from the LEX transitions from a burst, but organized, vortex to a wake-like flow at angles of attack beyond maximum lift. The decoupling mechanism occurs at all Mach numbers and limits the maximum yawing moment produced by the strake. The test data show that cropping the strake planform to account for structural and geometric constraints on the aircraft has only a small effect on the yaw control effectiveness at low subsonic speeds and virtually no effect at high subsonic and transonic speeds.

## Introduction

A major goal of the National Aeronautics and Space Administration (NASA) High-Angle-of-Attack Technology Program (HATP) (ref. 1) is to provide

design guidelines and new concepts for vortex control on advanced, highly maneuverable fighter aircraft. This program consists of wind tunnel testing of sub-scale models of complete aircraft configurations, sub-scale and full-scale models of aircraft components, piloted simulations, development and validation of computational fluid dynamics (CFD) methods, and full-scale flight testing. The flight experiments are performed with a highly instrumented F-18 aircraft as a High-Angle-of-Attack Research Vehicle (HARV) (ref. 2). As part of this research program, an actuated forebody strake concept has been developed (refs. 3 through 5) to provide increased levels of yaw control at high angles of attack where conventional aerodynamic control surfaces become ineffective. The concept features a pair of longitudinally hinged conformal strakes such as those sketched in figure 1. The results in references 3 through 5 show that the actuated strakes effectively modulate the forebody flow field and that the level of yaw control can be manipulated by varying the strake deflection. Ground-based studies of the actuated forebody strake control device applied to the F-18 configuration are underway (ref. 5), and these efforts will culminate in flight test demonstrations utilizing the NASA F-18 HARV.

In support of the forebody strake control ground-based studies, a wind tunnel investigation was conducted in the 7- by 10-Foot Transonic Tunnel at the David Taylor Research Center (DTRC) with a 0.06-scale model of the F/A-18 that was developed by the U.S. Navy, the McDonnell Douglas Corporation, and the Northrop Corporation with a strake mounted to the left side of the radome at  $120^\circ$  above the bottom centerline and normal to the surface. This configuration simulated the strake deployment leading to maximum yaw control at high angles of attack (ref. 4). A baseline, "gothic" planform strake (leading-edge sweep continuously increasing along the strake length) was tested along with a derivative cropped strake planform that was developed because of structural and geometric constraints on the aircraft. The principal objectives of the testing were to determine the effects of Mach number and strake planform (baseline versus cropped) on the strake yaw control effectiveness and the character of the strake-vortex-induced flow field at high angles of attack. These objectives were accomplished by conducting off-surface flow visualization with a laser vapor screen (LVS) technique and measuring the forebody and wing leading-edge extension (LEX) surface static pressure distributions and the six-component forces and moments of the complete model. Test data were obtained at free-stream Mach numbers

from 0.20 to 0.90, angles of attack from  $10^\circ$  to  $55^\circ$ , and angles of sideslip from  $-15^\circ$  to  $15^\circ$ . A flow visualization test was also conducted in the Langley 7- by 10-Foot High-Speed Tunnel to determine the strake effect on the surface flow patterns at subsonic speeds. The isolated forward-fuselage component (forebody, LEX's, and canopy) of the 0.06-scale F/A-18 model with an aft shroud assembly was used during this experiment. The surface flow patterns on the forward-fuselage-shroud model were correlated with trends in the LVS flow visualization and the surface static pressure distributions obtained on the complete 0.06-scale model in the DTRC facility.

## Symbols

$b$	reference wing span, 2.245 ft (0.06 scale)
$C_L$	lift coefficient, $\frac{\text{Lift}}{q_\infty S}$
$C_l$	body-axis rolling-moment coefficient, $\frac{\text{Rolling moment}}{q_\infty S b}$
$C_m$	pitching-moment coefficient referenced to $0.25\bar{c}$ , $\frac{\text{Pitching moment}}{q_\infty S \bar{c}}$
$C_n$	body-axis yawing-moment coefficient, $\frac{\text{Yawing moment}}{q_\infty S b}$
$C_p$	surface static pressure coefficient, $\frac{p-p_\infty}{q_\infty}$
$C_{p,u}$	upper surface static pressure coefficient
$C_Y$	side-force coefficient, $\frac{\text{Side force}}{q_\infty S}$
CFD	computational fluid dynamics
DTRC	David Taylor Research Center
$\bar{c}$	wing mean aerodynamic chord, 0.691 ft (0.06 scale)
c.g.	center of gravity
$d$	reference forebody diameter, 0.247 ft (0.06 scale)
$g$	gravitational acceleration, ft/sec <sup>2</sup>
FS	fuselage station, in. (full scale)
HARV	High-Angle-of-Attack Research Vehicle
HATP	High-Angle-of-Attack Technology Program
LEX	wing leading-edge extension
LVS	laser vapor screen
$M_\infty$	free-stream Mach number

NASA	National Aeronautics and Space Administration
$p$	local surface static pressure, lb/ft <sup>2</sup>
$p_o$	tunnel stagnation pressure, lb/ft <sup>2</sup>
$p_\infty$	free-stream static pressure, lb/ft <sup>2</sup>
$q_\infty$	free-stream dynamic pressure, lb/ft <sup>2</sup>
$\text{Re}_{\bar{c}}$	Reynolds number based on $\bar{c}$
$\text{Re}_d$	Reynolds number based on reference forebody diameter $d$
$S$	reference wing area, 1.440 ft <sup>2</sup> (0.06 scale)
$s$	local LEX semispan distance from LEX-fuselage junction to LEX leading edge, in. (full scale)
$T_o$	tunnel stagnation temperature, °F
WL	water line, in. (full scale)
$y$	distance along LEX local semispan, in. (full scale)
$\alpha$	angle of attack, deg
$\beta$	angle of sideslip, deg
$\delta_s$	forebody strake deflection angle relative to surface tangent, deg
$\theta$	forebody cross-section angular location ( $0^\circ$ is bottom dead center), deg
$\theta_s$	forebody strake angular location measured from bottom dead center, deg

## Experimental Investigation

### Model Description and Test Apparatus

The testing in the 7- by 10-Foot Transonic Tunnel at DTRC was conducted with a 0.06-scale model of the F/A-18 that was developed by the U.S. Navy, the McDonnell Douglas Corporation, and the Northrop Corporation, which is illustrated in figure 2. The model was tested with a leading-edge flap deflection of  $34^\circ$ , a trailing-edge flap deflection of  $0^\circ$ , a horizontal tail deflection (leading edge down) of  $-12^\circ$ , a rudder deflection of  $0^\circ$ , single-place canopy, and wingtip-mounted Sidewinder missiles. The model featured flow-through engine inlets. The outer fuselage contours aft of the twin vertical tails were distorted to allow the installation of a sting between the twin exhaust nozzles.

The forward fuselage, consisting of the forebody, LEX's, and canopy, was removable and was instrumented to measure surface static pressures at 93 pressure orifices on the forebody and 48 pressure orifices on the LEX's. The forebody pressures were measured

at FS 107, FS 142, and FS 184, and the LEX pressures were measured at FS 253, FS 296, and FS 357 as shown in figure 3. The fuselage stations are identical to those on the NASA F-18 HARV. The pressure port locations at each fuselage station on the 0.06-scale model are a subset of those on the aircraft.

A flat-plate, 0.031-inch-thick (0.06-scale) baseline strake with a symmetric (top and bottom) leading-edge bevel was mounted on the left side of the forebody at an angular position of  $120^\circ$  above the bottom centerline ( $\theta_s = 120^\circ$ ) and was normal to the forebody surface ( $\delta_s = 90^\circ$ ). The strake angular position and orientation are sketched in figure 4. In earlier low-speed ( $M_\infty = 0.08$ ) wind tunnel testing (ref. 4), this strake angular position and orientation with one strake deployed and one strake retracted generated the largest yaw control increments. The relative positions of the strake and the forebody pressure stations are also shown in figure 4. The baseline strake planform is sketched in figure 5(a) and resulted from designing a conformal strake that was as large as possible and would still fit within the radome area (ref. 4). The cropped strake was also tested at the same location and orientation. The cropped strake planform is sketched in figure 5(b) and was developed as a derivative of the baseline strake because of structural and geometric constraints on the aircraft. The forward end of the strake was cropped because of volume limitations at the apex of the forebody and to allow for the placement of a structural ring frame ahead of the strake. The aft end of the strake was shortened (cropped) to avoid interference with aircraft emergency systems and to allow placement of a ring frame aft of the strake.

The six-component forces and moments of the complete model were measured with an internally mounted strain-gauge balance. Pitch and yaw angle measurement devices were installed in the model support system, and the measurements were corrected for balance and sting deflection caused by the aerodynamic loads. The ceiling and floor in the test section of the DTRC facility are slotted. Blockage and wall interference corrections were not applied to the test data because of the relieving effect of the test section slots. However, data are unavailable from the DTRC facility to corroborate the assumption of negligible model blockage and tunnel wall interference at the very high angles of attack tested in the present experiment. The moment reference center location was FS 458.56 (25 percent of the mean aerodynamic chord) and WL 100.0. Model base and chamber pressures were measured. However, the model forces and moments were uncorrected for base/chamber or inlet duct flow effects. Drag measurements are not

shown in the present paper because of the emphasis on high-angle-of-attack stability and controllability.

The DTRC high-angle-of-attack sting was used in combination with the main boom support arrangement as shown in figure 6. Angles of attack from  $10^\circ$  to  $20^\circ$  were obtained by rotating the model about the pivot point of the main support system boom. Rotating about the high-angle-of-attack sting pivot point provided angles of attack from  $20^\circ$  to  $55^\circ$ . Within the latter angle-of-attack range, the model moved continuously upward through the test section. The model nose was approximately 9 in. from the slotted ceiling of the test section and was outside the ceiling boundary layer throughout the test angle-of-attack range.

The surface flow visualization testing in the Langley 7- by 10-Foot High-Speed Tunnel (7- by 10-Foot HST) was conducted with the 0.06-scale forward fuselage mounted to an aft shroud component as shown in figure 7. The forward-fuselage section consisted of the forebody, single-place canopy, and LEX's. The cross section of the shroud was constant and matched the cross section of the forward fuselage at FS 435.5. This configuration was tested in support of CFD method validation in the NASA HATP and resembled a computational representation of the F-18 forward-fuselage component that was used in reference 6.

The forward-fuselage-shroud model was tested without the baseline forebody strake and with the strake installed at an angular position of  $120^\circ$  above the bottom centerline. The strake was installed on the right side of the forebody during the testing in the Langley 7- by 10-Foot HST. This enabled the observation and documentation of the surface flow in the strake region with a video camera mounted on the same side of the tunnel test section which had suitable optical access.

The forward-fuselage-shroud configuration was nonmetric and was mounted to a sting by using a "dummy" balance assembly. The model pitch angle was measured by an accelerometer installed in the aft shroud.

### Flow Visualization Techniques

Off-body flow visualization was conducted on the complete 0.06-scale F/A-18 model in the 7- by 10-Foot Transonic Tunnel at DTRC by using a vapor screen technique (ref. 7). Water was injected into the settling chamber from a spray nozzle to increase the relative humidity level in the test section. The condensed water vapor patterns about the model were illuminated with an intense sheet of

laser light. The flow visualization technique is referred to accordingly as laser vapor screen (LVS). The water vapor condensed within the vortical flows at subsonic speeds. Illumination of the cross flow with the laser light sheet revealed bright vortices with a darker background. Water vapor condensation first occurred in the free stream at the transonic speeds, and the vortex flows appeared as dark regions in a light background. A combination of the two condensation patterns frequently occurred at high subsonic speeds. The model was painted flat black to reduce the reflection of laser light and to provide adequate contrast with the cross-flow patterns. The 6-W argon-ion laser was located outside the tunnel plenum shell because of operational considerations. A 150-ft fiber optic cable having a 200- $\mu\text{m}$  core diameter was used to deliver the laser beam to the light-sheet-generating optics positioned in the ceiling of the test section. The capability existed to remotely control the light-sheet thickness, divergence angle, and position along the model. The optics package was necessarily compact to allow installation in the limited space within the ceiling box beam. As a result, the light sheet was directed toward the test section by means of a miniature rotator stage and mirror assembly, which swept the light sheet in an arc along the model. A video camera with remotely controlled zoom lens was mounted to a tilt/pan mechanism situated outside the test section. The flow field was observed through a window in a right, three-quarter rear position. A video camera having a lens with a fixed focal length was mounted to the model sting support system and viewed directly between the twin vertical tails of the F/A-18 model. The field of view of this camera was fixed and was independent of the angles of attack and sideslip.

Surface flow visualization was conducted on the 0.06-scale F/A-18 forward-fuselage-shroud assembly in the Langley 7- by 10-Foot HST by using a mixture of titanium dioxide and mineral oil (ref. 8). The mixture was painted on the model prior to the run. Sufficient time was allowed during the run for the flow to become fully established. The real-time development of the flow was documented with a video camera outside the test section.

The photographs of the off-surface and on-surface flow visualizations presented in this paper were obtained from the original videotapes by using a video printer unit.

### Wind Tunnel Facilities and Test Conditions

The laser vapor screen flow visualizations and model force, moment, and surface static pressure

measurements were obtained in the 7- by 10-Foot Transonic Tunnel at DTRC in Bethesda, Maryland. The DTRC facility is a continuous-flow, closed-circuit facility capable of operating over a Mach number range of 0.20 to 1.17 and an equivalent pressure altitude range from sea level to 40 000 ft. A complete description of the transonic wind tunnel is provided in reference 9. The 0.06-scale F/A-18 model mounted in the test section of the DTRC facility is shown in figure 8. The test results were obtained at  $M_\infty = 0.20$  to 0.90,  $Re_c = 0.926 \times 10^6$  to  $1.728 \times 10^6$ ,  $Re_d = 0.331 \times 10^6$  to  $0.618 \times 10^6$ ,  $\alpha = 10^\circ$  to  $55^\circ$ , and  $\beta = -15^\circ$  to  $15^\circ$ . The maximum free-stream dynamic pressure during the test was approximately 250 lb/ft<sup>2</sup> because of a normal-force limit of 1000 lb imposed on the DTRC high-angle-of-attack support mechanism. For free-stream Mach numbers of 0.20 to 0.40, the testing was conducted at atmospheric conditions. The tunnel was operated in the evacuated mode (ref. 9) at the higher Mach numbers. The tunnel stagnation pressure varied with the Mach number but was typically less than 900 lb/ft<sup>2</sup> at  $M_\infty = 0.60$  to 0.90. The range of wind tunnel test conditions is given in the following table:

$M_\infty$	$p_o$ , lb/ft <sup>2</sup>	$T_o$ , °F	$Re_c$	$Re_d$
0.20	2090	68	$0.926 \times 10^6$	$0.331 \times 10^6$
0.40	2125	84	$1.728 \times 10^6$	$0.618 \times 10^6$
0.60	873	88	$0.974 \times 10^6$	$0.348 \times 10^6$
0.80	873	94	$1.140 \times 10^6$	$0.408 \times 10^6$
0.90	830	125	$1.064 \times 10^6$	$0.380 \times 10^6$

Surface flow patterns were obtained on the F/A-18 forward-fuselage-shroud model in the Langley 7- by 10-Foot High-Speed Tunnel. The Langley facility is a continuous-flow, subsonic-transonic atmospheric wind tunnel with solid test section walls. The Mach number range is from  $M_\infty \approx 0.06$  to 0.94 depending on model size. The tunnel operates at ambient temperature and pressure and continuously exchanges air with the surrounding atmosphere. Reference 10 provides a detailed description of the Langley facility. The model is shown mounted in the test section in figure 9. Surface flow visualization was conducted at  $M_\infty = 0.40$  for  $\alpha = 40^\circ$  and  $\beta = 0^\circ$ .

The complete 0.06-scale F/A-18 model tested in the 7- by 10-Foot Transonic Tunnel at DTRC featured boundary-layer transition strips on the forebody, LEX's, wings, tails, and inlet ducts. The transition strips consisted of small epoxy cylinders that

were bonded to the model surface. The epoxy cylinders had a nominal diameter of 0.05 in., spacing between cylinders of 0.025 in., and height of 0.0035 in. (0.06 scale). A transition ring was applied to the forebody about 0.40 in. (0.06 scale) from the nose tip, and a transition strip was installed along the entire forebody length at the bottom centerline. The transition strips on the LEX's, wings, tails, and inlet ducts were located 0.40 in. aft of the component leading edges. The 0.06-scale F/A-18 forward-fuselage-shroud model was tested in the Langley 7- by 10-Foot High-Speed Tunnel without transition strips.

## Discussion of Results

### Baseline Strake Results at Subsonic and Transonic Speeds

**Off-surface flow visualization.** Representative LVS flow visualization results obtained with the baseline strake mounted to the left side of the forebody for  $\theta_s = 120^\circ$  and  $\delta_s = 90^\circ$  are presented in this section. The model flow field is viewed from a three-quarter rear position and from the model support system looking upstream between the twin vertical tails. The vortical flows are illuminated by the wind tunnel test section lights located in the corner fillets, which provide a three-dimensional perspective of the condensation patterns, and by the laser light sheet, which yields flow-field cross sections. Reference is also made to the original LVS videotapes to augment the analysis of the off-surface flow visualization.

At  $M_\infty = 0.40$ , real-time observation of the flow field indicates that water vapor in the free stream first condenses in the strake vortex at an angle of attack of approximately  $22^\circ$ . Once this occurs, the strake vortex is visible along most of the model length. Onset of local condensation in the LEX vortices is at  $\alpha = 10^\circ$ . The LEX vortices are stronger than the forebody strake vortex and, consequently, are first visible at a lower angle of attack at this Mach number. Factors contributing to the higher strength of the LEX vortices include the longer generating length of the LEX's, the wing-induced upwash field, and the positive incidence angle of the LEX's with respect to the wing reference plane. The photographs in figure 10 show the off-surface flow field from a three-quarter rear position at  $\alpha = 20^\circ$  (fig. 10(a)), where the strake vortex is not visible, and at  $\alpha = 25^\circ, 30^\circ, 35^\circ$ , and  $40^\circ$  (figs. 10(b)–(f)), where the strake vortex is a prominent feature of the off-surface flow. The videotape documentation of the flow field at angles of attack of  $25^\circ$  and higher indicates that the strake vortex starts to lift away from the forebody surface just downstream of the strake

trailing edge. The upward displacement of the vortex core is amplified farther aft. As a result, the strake vortex core does not directly interact with the LEX vortices or the vertical tails. Increasing the angle of attack increases the distance of the strake vortex from the model surface. The decoupled nature of the strake vortex core and its upward movement with increasing angle of attack are apparent in figures 10(b) and 10(d)–(f). These trends are also apparent in figures 11 through 13, which show the vortex cross-flow patterns observed from the model support system for  $\alpha = 25^\circ, 30^\circ$ , and  $35^\circ$  and selected light-sheet locations.

The strake vortex induces an asymmetry in the LEX vortex cross-flow pattern. The LEX vortex on the side of the model opposite the deployed strake exhibits a larger cross section and an earlier breakdown over the wing, as illustrated in figures 11(c) and 12(a). This trend suggests that the strake-vortex-induced flow causes an increase in the local angle of attack at the LEX. The LVS videotapes indicate that the LEX vortex persists to a higher angle of attack with the forebody strake off. This effect is apparent even at angles of attack beyond maximum lift ( $\alpha > 40^\circ$ ), where vortex bursting advances toward the LEX apex. The flow-field observations are referred to in later sections that discuss differences in the model forces and moments and LEX surface pressures caused by the strake.

The vortex flow behavior is qualitatively, or topologically, similar at higher Mach numbers. However, quantitative differences exist between the vortex flows at subsonic and transonic speeds. The experimental results in reference 11 on the 0.06-scale F/A-18 model with the forebody strake off indicate that the LEX vortices induce locally supersonic flow beginning at a free-stream Mach number of approximately 0.60. The LEX vortices are weaker and their cross section is flatter at the higher Mach numbers. In addition, the vortices interact with shock waves over the main wing at the transonic speeds. Figure 14 shows the LVS cross-flow patterns observed from a three-quarter rear position at  $M_\infty = 0.80$  and  $\alpha = 20^\circ, 25^\circ, 30^\circ$ , and  $35^\circ$ . The strake vortex is first visible at a lower angle of attack at  $M_\infty = 0.80$  than at  $M_\infty = 0.40$ ; this is apparent by comparing the off-surface flow at  $\alpha = 20^\circ$  in figures 10(a) and 14(a) at  $M_\infty = 0.40$  and  $0.80$ , respectively. This result is typical of vortex flow behavior observed with the LVS technique (ref. 12) and suggests that lower temperatures and pressures exist within the vortex at higher Mach numbers that cause earlier condensation of the water vapor. The cross-flow patterns observed from the model support

system at  $\alpha = 20^\circ$  in figure 15 indicate that the strake vortex core is drawn toward the surface and interacts directly with the LEX vortices in the vicinity of the vertical tails. The direct interaction of the vortex cores is eliminated when the angle of attack increases to  $25^\circ$  as revealed in the photographs in figure 16. This result is representative of the observed vortex flow at all Mach numbers. The decoupled nature of the strake vortex core at higher angles of attack is clearly seen in the photographs shown previously at  $\alpha = 30^\circ$  and  $35^\circ$  in figures 14(c) and 14(d), respectively.

The LVS flow visualization results presented thus far have revealed the trajectory of the baseline strake vortex downstream of the forebody and the strake-vortex-induced effect on the LEX vortex cross flow. An indication of the strake effect on the separated flow field generated by the forebody is provided in figure 17, which presents the cross-flow patterns with strake off and strake on at  $\alpha = 40^\circ$  and  $M_\infty = 0.80$  observed from the model support system. Angles of attack above  $35^\circ$  at Mach numbers of approximately 0.80 and higher would be unobtainable because of aircraft structural  $g$  limits. The LVS patterns at  $M_\infty = 0.80$  are presented because of their increased clarity compared with the results obtained at lower Mach numbers. Examination of the LVS videotapes at  $M_\infty = 0.60$  to  $0.90$ , where limited details of the separated flow about the forebody are discerned with this flow visualization technique, shows that the vortex positioning is similar at subsonic and transonic speeds. The forebody flow is sensitive to the Mach number, however. The test data on the 0.06-scale F/A-18 model without strake in reference 11 indicate that the separation of the primary boundary layer along the forebody occurs sooner when the Mach number increases. This effect strengthens the forebody primary vortex system. Supersonic regions exist along the forebody at the high angles of attack beginning at a free-stream Mach number of about 0.80, and shock waves may exist that affect the location of primary boundary-layer separation. With the strake off, a symmetric pair of counterrotating forebody vortices is manifested in the cross-flow pattern in figure 17(a). The forebody vortices appear as small, white “dots” situated close to the model surface and on either side of the top centerline. The LEX vortices appear as larger lobe-shaped regions lacking in water vapor condensate. The cross-flow pattern is asymmetric with the strake on (fig. 17(b)). The strake vortex is situated high above the surface and to the left of the model centerline. A second vortex, rotating in the opposite sense, is generated from the side of the forebody op-

posite the deployed strake. This vortex is in proximity to the model surface and is near the top centerline at this fuselage station. The forebody vortex is larger, and the level of reflected light from the water vapor condensate is higher compared with that for the strake off. The LVS observations are insufficient to evaluate the net circulation about the forebody. However, these results suggest that the strake vortex induces a circulation of opposite sense about the forebody, which promotes a stronger vortex on the side of the forebody opposite the strake. Furthermore, the orientation of the vortices with the strake on is consistent with a delay of primary boundary-layer separation on the side of the forebody opposite the strake. The increased suction caused by the attached flow would be expected to produce a net side force and yawing moment in the direction away from the strake. The experimental results obtained in reference 13 on a fighter forebody have shown that the orientation of the forebody vortices is a qualitative indicator of the sign of the yawing moment. For example, yawing moments are generated in the direction toward the side of the forebody where the vortex is closest to the surface.

As a result of its proximity to the surface, the vortex that is generated from the side of the forebody opposite the strake is coupled to the LEX vortical flows. The photographs obtained from the model support system camera in figure 18 at  $\alpha = 40^\circ$  and  $M_\infty = 0.80$  indicate that the forebody vortex is stretched and compressed as it passes between the LEX vortices, which have burst upstream of the light-sheet stations. The LVS videotapes show that the LEX vortices are stable, however, along the forward portion of the LEX. The forebody vortex definition is lost farther aft on the model (fig. 18(c)) because of its downward and outboard entrainment underneath the LEX vortex on the side of the model opposite the strake.

Analysis of the flow visualization videotapes at subsonic and transonic speeds shows that the LEX vortex breakdown advances forward to the LEX apex at  $\alpha = 50^\circ$ ; this has also been observed in flight on the NASA F-18 HARV (ref. 14). At higher angles of attack, a wake-like flow is shed from the LEX and coincides with a decoupling of the forebody vortex from the LEX flow field. The LVS photographs in figure 19 show the cross-flow patterns observed from the model support system at a fuselage station downstream of the canopy for  $M_\infty = 0.80$  and  $\alpha = 40^\circ$  and  $50^\circ$ . At  $\alpha = 40^\circ$  (fig. 19(a)), the forebody vortex generated from the strake-off side of the forebody is coupled to the LEX vortical flows. At  $\alpha = 50^\circ$  (fig. 19(b)), however, the forebody vortex is positioned far above

the surface and in proximity to the strake vortex. No visible water vapor condensate is present in the region above the LEX's. The flow visualization results obtained from a three-quarter rear position for  $M_\infty = 0.60$  and  $\alpha = 50^\circ$  and  $55^\circ$  in figure 20 reveal a similar trend, although the forebody vortex decoupling occurs at a higher angle of attack at  $M_\infty = 0.60$  than at  $M_\infty = 0.80$ . At  $\alpha = 55^\circ$  and  $M_\infty = 0.60$ , bursting of the forebody vortex occurs aft of the canopy. These flow mechanisms would be expected to limit the maximum yawing moment produced by the strake. This trend is discussed in the section "Longitudinal and lateral-directional characteristics."

The sensitivity of the cross-flow patterns to sideslip from the perspective of the downstream video camera is shown in figure 21 for  $M_\infty = 0.80$  and  $\alpha = 40^\circ$ . Positive sideslip is defined as a nose left orientation as viewed from the downstream camera. For this figure, the strake is on the leeward side of the forebody. The light sheet is positioned over the canopy and reveals the strake vortex and the forebody vortex shed from the side opposite the strake. The strake vortex is smaller and farther outboard at  $\beta = 8^\circ$  (fig. 21(a)) when compared with  $\beta = 0^\circ$  (fig. 21(b)). In addition, the forebody vortex is slightly larger, higher above the surface, and crosses over to the leeward side of the top centerline. The trend is the opposite at  $\beta = -8^\circ$  (fig. 21(c)). The relative positioning of the strake and forebody vortices is similar within the range of sideslip angle from  $\beta = -8^\circ$  to  $8^\circ$ ; the forebody vortex opposite the strake-deployed side remains closest to the surface. As a result, the cross-flow patterns suggest that yawing moments in the direction opposite the deployed strake occur within this range of sideslip angle. Sensitivity of the forebody vortex behavior to small changes in the sideslip angle was observed at  $\alpha = 50^\circ$  and  $M_\infty = 0.60$ , as shown in the photographs obtained from the downstream video camera in figure 22. The light sheet is positioned over the canopy. The forebody vortex at  $\beta = 4^\circ$  (fig. 22(a)) is burst and is situated far above the surface. At  $\beta = 6^\circ$  (fig. 22(b)), however, the vortex stabilizes and moves closer to the surface in response to the change in the LEX flow field from a wake-like structure to a burst, but organized, vortex flow.

**Surface flow visualization.** Surface flow patterns for strake off and strake on at  $\alpha = 40^\circ$  and  $M_\infty = 0.40$  are shown in figures 23 and 24. This testing was conducted with the 0.06-scale forward-fuselage-shroud assembly in the Langley 7- by 10-Foot High-Speed Tunnel. The baseline strake is mounted to the right side of the forebody as

opposed to the tests at DTRC. Primary boundary-layer separation occurs earlier on the side of the forebody with deployed strake (fig. 23(b)). A recirculation region, or separation "bubble," exists underneath the strake. Lines of primary and secondary boundary-layer separation are apparent below the strake and along the region of the forebody downstream of the strake. The primary vortex associated with these separation lines is small and weak and was not visible in the LVS flow visualization on the complete 0.06-scale model tested in the DTRC facility at any Mach number. The footprint of the strake vortex is identified in the surface streamlines along the lee side of the forebody in figure 24(b). Near the canopy, however, the strake vortex footprint is smeared because of the upward displacement of the vortex away from the surface, which was observed in the LVS flow visualizations. With the strake off, the surface flow patterns in figure 24(a) reveal two secondary separation lines positioned symmetrically along either side of the top centerline. These separation lines are associated with the forebody primary vortex pair that was discussed in reference to the LVS photograph in figure 17(a) at  $M_\infty = 0.80$ . In contrast, the dominant feature of the surface flow with the strake on is the single secondary separation line that tracks along the center region of the forebody and canopy (fig. 24(b)). This is consistent with the strong primary vortex from the strake-off side of the forebody that was illustrated previously in the flow-field photograph at  $M_\infty = 0.80$  in figure 17(b). (Note that the strake is on the left side of the forebody in the DTRC test.) Figure 25 shows the surface streamline patterns on the left and right sides of the forebody with the strake on for  $M_\infty = 0.40$  and  $\alpha = 40^\circ$ . These results show that primary boundary-layer separation occurs much higher on the forebody on the strake-off side. The trends in the experimental surface patterns are similar to the surface streamlines on the F-18 forebody with strake computed by using the Navier-Stokes method of reference 15. Comparison of the surface streamlines obtained at a subsonic speed with the off-surface flow-field trends observed at high subsonic and low transonic speeds indicates that the qualitative effects of the strake on the vortex-dominated flow field are similar.

**Longitudinal and lateral-directional characteristics.** Figures 26 and 27 show the baseline strake effect on the longitudinal and lateral-directional characteristics at  $M_\infty = 0.40$  and  $\beta = 0^\circ$ . Adding the strake increases the lift at angles of attack from  $10^\circ$  to  $50^\circ$  and promotes nose-up pitching-moment increments at  $\alpha \approx 25^\circ$  to  $50^\circ$  (fig. 26). These effects are relatively small and are caused by

the projected area increase and strake vortex lift which act ahead of the moment reference center. At  $\alpha = 55^\circ$ , the strake decreases the lift and causes a nose-down pitching-moment increment. This correlates with the forebody vortex decoupling and vortex breakdown phenomena that were observed at higher Mach numbers in the LVS flow visualizations.

Adding the strake causes small positive yawing-moment increments at  $\alpha = 10^\circ$  and  $15^\circ$  (figs. 27(a) and (b)). The side-force increments are negative at these angles of attack. LVS flow visualization results were not obtained in the testing of the 0.06-scale F/A-18 model for these angles of attack at  $M_\infty = 0.40$ . However, the cross-flow patterns observed at the higher Mach number show that the strake vortex core interacts directly with the LEX vortex core, and this strake-LEX vortex system interacts with the vertical tails. The observed strake vortex path is close to the fuselage and between the twin tails. It is hypothesized that the positive increments to the yawing moment and the negative increments to the side force at these angles of attack are caused by the vortex-induced flow at the tail surfaces and a direct suction effect induced by the strake vortex on the forebody. However, low-speed ( $M_\infty = 0.08$ ) wind tunnel testing on a 0.16-scale F/A-18 model did not exhibit these trends. (See ref. 4.) The positive slope of the yawing-moment curve with the strake on exhibits a significant increase at  $\alpha = 20^\circ$ , and the strake produces very high levels of yawing moment at higher angles of attack. The strake yaw control effectiveness is maximum at  $\alpha = 50^\circ$  and then diminishes by about 35 percent at  $\alpha = 55^\circ$ . The side force produced by the strake is in the same direction as the yawing moment at  $\alpha \geq 20^\circ$ ; that is, a side force to the right produces a yawing moment to the right. These results are consistent with the LVS flow-field observations (fig. 10) that show the strake vortex is positioned high above the model surface and does not directly interact with the flow about the LEX, wing, or tail surfaces. Relative to the yawing-moment results, the side force peaks at a lower angle of attack ( $45^\circ$ ) and then decreases rapidly at higher angles of attack. The yawing moment and side force trends at angles of attack of  $20^\circ$  and greater are similar to those observed in the low-speed testing of the 0.16-scale F/A-18 model in reference 4. The increase in the yawing moment despite the side force decrease at  $\alpha = 50^\circ$  indicates a forward shift in the center of pressure of the side load on the forebody. The expected effect of the observed decoupling of the forebody vortex from the LEX vortex on the strake-off side is to reduce the suction pressures and, consequently, the local side force along the

canopy and the rear portion of the forebody. Farther forward, however, the strake-vortex-induced effect on the local side force and its corresponding large moment arm are maintained. The concurrent drop-off in the yawing moment and side force at  $\alpha = 55^\circ$  coincides with the development of a wake-like flow shed from the LEX's and a corresponding large upward displacement and breakdown of the forebody vortex. This effect was shown in the LVS photographs in figure 20.

The data in figure 27 show that the strake produces asymmetric rolling moments beginning at  $\alpha \approx 25^\circ$ . The sense of the asymmetry changes with increasing angle of attack. The LVS videotapes indicate that the strake vortex induces an asymmetry in the LEX-wing flow field even at the lower angles of attack; however, this effect is too small to cause any measurable rolling moment. At higher angles of attack, the strake vortex induces a circulation of opposite sense about the forebody that is sufficient to increase the local upflow at the LEX on the strake-off side. The LEX vortex is stronger which increases the vortex-induced lift on the wing. As the angle of attack increases, the higher local upflow renders the LEX vortex more susceptible to breakdown. As a result, the vortex-induced lift on the wing diminishes. These trends contribute to the cyclic variation of rolling moment with angle of attack. The rolling moments are relatively small and can be countered by aileron deflection (ref. 4).

Figures 28 through 31 present the strake effect on the longitudinal and lateral-directional characteristics for  $M_\infty = 0.60$  and  $0.80$  and  $\beta = 0^\circ$ . The trends at the higher Mach numbers are similar to those observed at  $M_\infty = 0.40$ . The maximum yawing moments produced by the strake are smaller, however. The yaw control effectiveness peaks at a lower angle of attack ( $45^\circ$ ) at  $M_\infty = 0.80$  (fig. 31(a)). This effect is consistent with the LVS flow visualizations, which revealed an earlier onset of the forebody vortex decoupling at  $M_\infty = 0.80$  (fig. 19).

The results at  $M_\infty = 0.40$  to  $0.80$  in figures 26 through 31 show that the strake produces small coupled pitching moments and rolling moments and acts essentially as a decoupled yaw control device at angles of attack greater than  $20^\circ$ . These results agree with the vortical flow-field trends discussed in the previous section.

The effect of the Mach number on the strake yaw control effectiveness is shown in figure 32. The strake yaw control is apparent at all Mach numbers from  $M_\infty = 0.20$  to  $0.90$  at angles of attack greater than  $20^\circ$ . At  $M_\infty = 0.20$  to  $0.60$ , maximum yawing

moments are reached at  $\alpha = 50^\circ$ , followed by a drop-off in the yaw control at  $\alpha = 55^\circ$ . At the higher Mach numbers ( $M_\infty = 0.80$  and  $0.90$ ), the yawing moments exhibit a maximum plateau beginning at  $\alpha = 45^\circ$ . The yawing moments generated by the strake at a given angle of attack decrease with increasing Mach number at  $\alpha = 25^\circ$  to  $50^\circ$ . The reductions in control effectiveness are relatively minor from  $M_\infty = 0.20$  to  $0.60$  but are more significant from  $M_\infty = 0.60$  to  $0.90$  at angles of attack above  $\alpha = 35^\circ$ . The strake vortex strength diminishes with increasing Mach number, particularly in the transonic regime. In references 11, 16, and 17, the observation is that the vorticity shed from sharp leading edges of strakes and wings diminishes as Mach number increases; this causes a reduction in the vortex strength. In contrast, vortex strength may increase with Mach number on smooth bodies and surfaces with blunt leading edges (ref. 18). This increase is caused by earlier boundary-layer separation which may be shock induced at the higher Mach numbers. This trend is analogous to the sensitivity of the vortex development to Reynolds number about these classes of aerodynamic shapes (ref. 19). For example, the vortices are larger and stronger at lower Reynolds numbers because the laminar boundary layer separates from the surface sooner than for the turbulent boundary layer. The circulation induced about the forebody by the strake vortical flow will decrease at the higher Mach numbers. Despite the influence of compressibility on the strake yaw control effectiveness, the yawing moments generated by the strake at all Mach numbers exceed the low-speed rudder effectiveness at  $\alpha > 30^\circ$  (ref. 4). The rolling moments caused by the strake are relatively small and do not exceed the low-speed aileron effectiveness (ref. 4).

Figures 33 through 35 show the strake effectiveness at sideslip for  $M_\infty = 0.60$  and  $\alpha = 30^\circ$ ,  $40^\circ$ , and  $50^\circ$ . Several repeat data points were obtained at each sideslip angle to evaluate unsteady flow effects on the time-averaged lateral-directional characteristics. The strake provides yaw control increments over wide ranges in sideslip at the angles of attack shown. The model with strake off exhibits a nonlinear variation of the yawing moment with sideslip at  $\alpha = 30^\circ$  (fig. 33(a)). This effect is attributed to the interaction of the LEX vortices with the twin vertical tails. Adding the strake does not affect the interaction of the LEX vortex and tail or the character of the yawing-moment curve at this angle of attack. The yawing-moment and side-force data obtained at  $\alpha = 40^\circ$  and  $M_\infty = 0.60$  with strake off show significant scatter at a given sideslip angle (figs. 34(a) and (b)). The vertical tails are blanketed by the

burst LEX vortices and lower energy wake from the wings at this angle of attack. The data scatter is caused by the loss of vertical tail effectiveness and the interaction of the unsteady separated flow from the LEX's and wings with the vertical tails. Adding the strake promotes a steady vortex-dominated flow about the forebody that causes large yaw control increments, a more linear variation of yawing moment with sideslip, and a significant reduction in the data scatter.

The strake effect is similar at  $\alpha = 50^\circ$  (fig. 35), although somewhat less linear yawing-moment characteristics are obtained compared with the data at  $\alpha = 40^\circ$  (fig. 34). The LVS flow visualizations at  $\alpha = 50^\circ$  (fig. 22) show that the interaction of the forebody vortex on the side opposite the strake and the LEX vortex is sensitive to changes in sideslip angle. At angles of attack beyond maximum lift, the LEX vortex is prone to change from a burst, but organized, rotating flow near the LEX apex to a wake-like flow. This effect decouples the forebody vortex from the LEX flow. The movement of the forebody vortex away from the body decreases the strake yaw control increment. For example, the discontinuity in the yawing-moment curve between  $\beta = 4^\circ$  and  $6^\circ$  (fig. 35(a)) correlates with observed flow-field trends (fig. 22). The forebody vortex is decoupled from the wake-like flow from the LEX at  $\beta = 4^\circ$ . Increasing the sideslip angle beyond  $4^\circ$  causes a downward movement and intensification of the forebody vortex and a corresponding reestablishment of a burst vortex above the LEX.

The yawing-moment increments caused by the strake at a given angle of attack are typically larger at negative sideslip angles (nose right), where the strake is on the windward side of the forebody. In this case, the strake vortex is closer to the forebody surface compared with its position at positive sideslip angles (nose left) (fig. 21) and will induce a corresponding greater circulation about the forebody.

The strake has little effect on the rolling-moment variation with sideslip for  $M_\infty = 0.60$  at  $\alpha = 30^\circ$  and  $40^\circ$  (figs. 33(c) and 34(c)). The model exhibits neutral lateral stability for  $\alpha = 40^\circ$  and small sideslip angles with strake off and strake on. The strake promotes an increase in lateral stability and a more linear variation of the rolling moment with sideslip at  $\alpha = 50^\circ$  (fig. 35(c)) compared with the effects for strake off.

The strake effectiveness at sideslip for  $M_\infty = 0.80$  and  $\alpha = 30^\circ$  and  $40^\circ$  is shown in figures 36 and 37. The strake yaw control increments at  $M_\infty = 0.80$  exhibit a trend similar to that obtained at

$M_\infty = 0.60$ . The scatter in the yawing-moment and side-force data that is apparent at  $M_\infty = 0.60$  and  $\alpha = 40^\circ$  (figs. 34(a) and (b)) with strake off is significantly less at  $M_\infty = 0.80$  (figs. 36(a) and (b)). Reference 11 indicates that the forebody vortices on the 0.06-scale F/A-18 model are stronger at  $M_\infty = 0.80$  than at  $M_\infty = 0.60$ . Furthermore, the development of cross-flow shock waves along the sides of the forebody may “fix” the location of primary boundary-layer separation at the high angles of attack. These effects may oppose unsteadiness in the yaw plane at  $M_\infty = 0.80$ .

The strake increases the nonlinear variation of rolling moment with sideslip for  $M_\infty = 0.80$  and  $\alpha = 30^\circ$  and  $40^\circ$  (figs. 36(c) and 37(c)). The flow-field asymmetry and corresponding asymmetric rolling moment caused by the strake at  $\beta = 0^\circ$  lead to large changes in the lateral stability at small sideslip angles.

**Forebody surface static pressure distributions.** The baseline strake effect on the forebody surface static pressure distributions at  $M_\infty = 0.40$  and FS 107, FS 142, and FS 184 is presented in figures 38 through 42 for  $\alpha = 20^\circ, 30^\circ, 40^\circ, 50^\circ$ , and  $55^\circ$ . The pressure distributions obtained on the side of the forebody opposite the deployed strake (strake-off side) and the side of the forebody with the strake (strake-deployed side) are plotted separately. The pressure distributions are plotted from the perspective of an observer standing behind the model looking forward (“pilot’s perspective”).

The strake effect on the forebody surface pressures at  $\alpha = 20^\circ$  (fig. 38) is small. A local suction pressure increase occurs underneath the strake vortex at FS 107. Otherwise, the strake promotes a slight decrease in the suction pressures below the strake and a slight increase in suction pressure level on the strake-off side of the forebody. At this angle of attack, the strake vortex strength is insufficient to induce large changes in the forebody pressure distributions. This is consistent with the inability to visualize the strake vortex at this angle of attack and Mach number using the LVS technique (fig. 10(a)) and the small yawing moment that was shown previously in figure 27(a).

The strake vortex surface pressure signature, or vortex footprint, at FS 107 increases with increasing angle of attack. This increase is shown in the pressure distributions at  $\alpha = 30^\circ$  and  $40^\circ$  in figures 39 and 40. The location of the strake-vortex-induced suction peak moves higher up on the forebody compared with that at  $\alpha = 20^\circ$  because of the growth and upward migration of the vortical flow. The vortex

is far enough from the surface at FS 142 that its pressure signature is no longer apparent at either angle of attack. The strake causes a net decrease in the suction pressure level on the strake-deployed side of the forebody and a suction pressure level increase on the strake-off side. The overall effect is to produce differential suction pressures that cause a side force and yawing moment in a direction opposite the deployed strake. The induced effect of the strake vortex on the forebody surface pressures increases with angle of attack because of the increased vortex strength. The deceleration of the flow below the strake is consistent with the early primary boundary-layer separation and the recirculation zone shown previously in the surface flow patterns in figure 23 for  $M_\infty = 0.40$  and  $\alpha = 40^\circ$ . Similarly, the flow acceleration on the opposite side of the forebody concurs with the delayed primary separation that was apparent in the surface streamlines in figure 25. The signature of the vortex shed from the strake-off side of the forebody is manifested in the pressure distributions at  $\alpha = 40^\circ$  and FS 184 (fig. 40(c)). The forebody vortex suction peak is situated at the top centerline ( $\theta = 180^\circ$ ), which is similar to the vortex location revealed in the LVS cross-flow pattern at  $M_\infty = 0.80$  in figure 17(b) and the surface streamlines at  $M_\infty = 0.40$  in figure 24(b).

Increasing the angle of attack to  $50^\circ$  (fig. 41) moves the strake vortex suction peak to a higher position on the forebody at FS 107. The magnitude of suction peak is unchanged compared with the result at  $\alpha = 40^\circ$ . This suggests that the increased vortex strength is offset by the upward migration of the vortical flow. The strake effect on the surface pressure increases at FS 107 and FS 142 compared with that at  $\alpha = 40^\circ$ . At FS 184, however, the net suction pressure increase on the strake-off side is less at  $\alpha = 50^\circ$ . The “peaking out” of the strake vortex pressure signature and the diminished effect of the strake on the surface pressures along the rear portion of the forebody coincide with the maximum yawing moment and drop-off in the total side force at  $\alpha = 50^\circ$  in figures 27(a) and (b).

At  $\alpha = 55^\circ$  (fig. 42), the strake vortex suction pressure peak at FS 107 is less compared with that at  $\alpha = 50^\circ$  (fig. 41). The suction pressure decrease below the strake is nominally greater at all three measurement stations at the higher angle of attack. The principal effect of increasing the angle of attack on the strake-off side is to decrease the suction pressure level at FS 184 compared with that for the strake off. The reversal of the pressure distribution trend at FS 184 and  $\alpha = 55^\circ$  is caused by the forebody vortex decoupling and breakdown phenomena that were

illustrated in the LVS photographs at  $M_\infty = 0.60$  in figure 20. This effect reduces the strake yaw control increment as shown previously in figure 27(a).

The trends are similar at higher Mach numbers. Figures 43 through 46 illustrate the strake effect on the forebody surface pressures at  $M_\infty = 0.80$  and  $\alpha = 20^\circ, 30^\circ, 40^\circ$ , and  $50^\circ$ , respectively. The ability of the strake to promote large changes in the suction pressure levels on both sides of the forebody diminishes at the higher Mach number. The forebody vortex footprint on the strake-off side is apparent in the pressure distributions for strake off and strake on at FS 142 and  $\alpha = 40^\circ$  (fig. 45(b)) and  $50^\circ$  (fig. 46(b)). The circulation induced by the strake vortex causes a stronger forebody vortex pressure signature compared with the pressure signature for the strake off. This effect is in qualitative agreement with the cross-flow patterns above the canopy in figure 17 for  $M_\infty = 0.80$  and  $\alpha = 40^\circ$ , which show a larger, better defined forebody vortex with strake on.

The Mach number effect on the forebody surface pressures with the strake on is illustrated in figures 47 and 48 at  $\alpha = 40^\circ$  and  $50^\circ$ , respectively. The strake vortex pressure signature at FS 107 (figs. 47(a) and 48(a)) decreases with increasing Mach number at both angles of attack. This decrease is caused by the diminished vortex strength at the higher Mach numbers (refs. 11, 16, and 17). This effect is most pronounced as the Mach number increases from  $M_\infty = 0.60$  to 0.80. As a result of the weaker strake vortex, the circulation of opposite sense induced about the forebody is reduced (fig. 47(b)). The region of the forebody that is most sensitive to the Mach number is on the side opposite the deployed strake. The flow acceleration and, consequently, the increased suction pressure levels diminish in response to the weaker strake vortex.

The principal effect of increasing Mach number from  $M_\infty = 0.20$  to 0.60 at  $\alpha = 40^\circ$  is seen at FS 184 (fig. 47(c)). At  $M_\infty = 0.80$  and 0.90, however, the Mach number effect is global and can be seen at all three measurement stations. At  $\alpha = 50^\circ$  (fig. 48), the Mach number effect becomes more significant at FS 107 and FS 142 at lower Mach numbers. However, maneuvers at this angle of attack are conducted at Mach numbers of 0.40 or less, where compressibility effects on the strake yaw control effectiveness are relatively small.

**LEX upper surface static pressure distributions.** The baseline strake effect on the LEX upper surface static pressure distributions is shown in figures 49 through 55 for  $M_\infty = 0.40$ ,  $\beta = 0^\circ$ , and selected angles of attack from  $20^\circ$  to  $55^\circ$ . The LEX

pressure distributions for the strake-deployed side and the strake-off side are presented from the perspective of an observer standing behind the model looking forward. The surface pressures are plotted against the local semispan distance  $y$  measured from the LEX-fuselage junction, normalized by the local distance  $s$  from the LEX-fuselage junction to the LEX leading edge. For the strake-deployed side, values of  $y/s$  of 0 and  $-1$  correspond to the LEX-fuselage junction and LEX leading edge, respectively. Similarly, values of  $y/s$  of 0 and 1 coincide with the LEX-fuselage junction and LEX leading edge on the strake-off side. The locations of the pressure orifices are the same on both sides at FS 253. There are two less pressure orifices on the strake-deployed side than on the strake-off side at FS 296 and FS 357.

The strake causes asymmetries in the LEX surface pressures at FS 253, FS 296, and FS 357 beginning at  $\alpha = 20^\circ$  (fig. 49). This effect coincides with the onset of the strake vortex footprint in the forebody surface pressures at  $\alpha = 20^\circ$  (fig. 38). The acceleration of the flow on the side of the forebody opposite the strake increases the local angle of attack at the LEX. This effect increases the strength and the corresponding surface pressure signature of the LEX vortex. The flow deceleration along the forebody on the strake-deployed side causes an opposite effect. Indicators of the differences in the local flow angle at the LEX's are provided in the LVS flow visualizations and surface flow patterns shown previously in figures 11 and 25, respectively. The LVS cross-flow images show a larger LEX vortex on the side opposite the strake, whereas the surface flow patterns reveal steeper local flow angles approaching the LEX apex on the strake-off side.

Increasing the angle of attack to  $25^\circ$  increases the strake vortex strength and the circulation of opposite sense induced about the forebody. As a result, the LEX surface pressure asymmetries increase (fig. 50). The LEX vortex is stronger on the strake-off side, and it induces higher suction pressure peaks. The stronger LEX vortex is prone to earlier breakdown, however, because it reaches a critical swirl angle sooner (ref. 20). This effect is not apparent in the pressure distributions in figure 50 but is revealed in the LVS cross-flow pattern near the LEX-wing junction at  $\alpha = 25^\circ$  in figure 12(a).

Vortex breakdown advances forward to the aft region of the LEX on both sides of the model at  $\alpha = 30^\circ$  (fig. 12(b)). As the angle of attack increases, the LEX surface pressure asymmetry induced by the strake vortex increases in regions unaffected by LEX vortex breakdown but diminishes in regions influenced by the burst vortex. The test results

for  $\alpha = 30^\circ$  (fig. 51) show that the vortex pressure signature asymmetry increases at FS 253 and FS 296 but decreases at FS 357 compared with the results at  $\alpha = 25^\circ$  (fig. 50).

The forward movement of the LEX vortex breakdown over the LEX's at  $\alpha = 35^\circ$  and  $40^\circ$  limits the LEX surface pressure asymmetries (figs. 52 and 53) induced by the strake vortex. The suction pressure asymmetry at  $\alpha = 40^\circ$  and FS 253 (fig. 53(a)) decreases compared with the results at  $\alpha = 35^\circ$  (fig. 52(a)). The maximum suction pressure levels are comparable on both sides of the model for  $\alpha = 40^\circ$  at FS 296 and FS 357.

The test results at  $\alpha = 50^\circ$  (fig. 54) indicate that the forward progression of the LEX vortex breakdown is more rapid on the strake-deployed side, where the pressure distributions are nearly uniform at all measurement stations. A suction pressure peak is maintained on the strake-off side at FS 253, which suggests a continued interaction between the forebody vortex and LEX vortex. The yaw control increment caused by the strake is maximum at  $\alpha = 50^\circ$  (fig. 27(a)).

The increased circulation induced by the strake vortex leads to a more dramatic breakdown of the flow field. This is analogous to vortex enhancement concepts such as spanwise blowing which increase vortex lift (ref. 21) but often cause a more abrupt stall. The LVS flow visualizations indicate that the movement of the strake and forebody vortices away from the surface and their subsequent breakdown at  $\alpha = 55^\circ$  are abrupt. This effect propagates downstream to cause a corresponding breakdown of the LEX vortex flows. There is no evidence in the LVS videotapes of a similar significant change in the forebody and LEX flow field behavior with strake off. In fact, the flow near the LEX apex retains an organized rotating character at  $\alpha = 55^\circ$ . The transition to a wake-like flow about both LEX's with the strake on at  $\alpha = 55^\circ$  is reflected in the pressure data in figure 55. The LEX surface pressures are uniform and approximately the same suction level at all measurement stations. In contrast, the LEX suction pressure levels with strake off are higher and indicate burst, but organized, rotating flows. The onset of a wake-like flow from the LEX's indicated by the flat pressure distributions, along with the forebody-LEX flow decoupling and breakdown revealed in the LVS flow visualizations (figs. 19 and 20), coincides with the decreased strake yaw control effectiveness at  $\alpha = 55^\circ$  (fig. 27(a)). Furthermore, the more rapid loss of LEX vortex lift with the strake on is consistent with the lower total lift and increased nose-down pitching moment compared with the strake off (fig. 26).

The trends in the LEX surface pressures and LVS flow visualizations are consistent with the asymmetric rolling moments at  $\beta = 0^\circ$  in figure 27. However, the LEX pressure distributions and cross-flow patterns are insufficient to assess relative lift levels on the wings and, consequently, the sign of the rolling moment.

The strake effect on the LEX surface pressures for  $M_\infty = 0.80$ ,  $\beta = 0^\circ$ , and selected angles of attack from  $\alpha = 20^\circ$  to  $50^\circ$  is presented in figures 56 through 62. The trends in the LEX surface pressure asymmetries caused by the strake at  $M_\infty = 0.80$  are similar to those observed at  $M_\infty = 0.40$  (figs. 49–55). The magnitude of the surface pressure asymmetry is less at the higher Mach number because of the weaker strake vortex. It is noted that the LEX vortex pressure signatures at higher Mach numbers typically do not exhibit the pronounced suction peaks that occur at lower Mach numbers (ref. 22). As a result, the onset of LEX vortex breakdown effects is more difficult to determine from the flatter pressure distributions at  $M_\infty = 0.80$ . Increasing the angle of attack from  $40^\circ$  (fig. 60) to  $45^\circ$  (fig. 61) causes a disproportionate decrease in the maximum suction pressure levels and flattens the pressure distributions on the strake-deployed side compared with the strake-off side. These results suggest that LEX vortex breakdown approaches the LEX apex more rapidly on the strake-deployed side. This flow situation coincides with the plateaus in the total lift (fig. 30(a)) and strake yaw control effectiveness (fig. 31(a)). The strake causes a large decrease in the LEX suction pressure levels on both sides of the model at  $\alpha = 50^\circ$  (fig. 62). In addition, the pressure distributions are uniform everywhere, except FS 253 on the strake-off side. These trends correlate with LVS flow visualizations which show a loss of an organized vortex about the LEX's and a decoupling of the forebody and LEX vortices on the strake-off side. The strake-vortex-induced flow mechanisms cause a lift loss and nose-down pitching-moment increment compared with the strake off (fig. 30) and a slight decrease in the strake yaw control effectiveness (fig. 31(a)). The transition from an organized burst vortex about the LEX's to a wake-like flow occurs at an angle of attack approximately  $5^\circ$  lower at  $M_\infty = 0.80$  than at  $M_\infty = 0.40$ .

### Strake Planform Effects

**Longitudinal and lateral-directional characteristics.** Figures 63 through 65 compare the lift and pitching-moment characteristics at  $M_\infty = 0.40$ ,  $0.60$ , and  $0.80$  with the baseline and cropped strakes mounted to the left side of the forebody at  $\theta_s = 120^\circ$

and  $\delta_s = 90^\circ$ . No effect of the strake cropping is apparent in the lift and pitching-moment curves except at  $M_\infty = 0.60$  and  $\alpha = 55^\circ$  (fig. 64). Here, cropping the strake promotes a slight lift increase and nose-up pitching-moment increment. The LVS videotapes of the baseline and cropped strakes reveal a less abrupt decoupling of the forebody vortex and LEX vortex with the cropped strake. However, this effect was not apparent at other Mach numbers.

The lateral-directional characteristics obtained with the baseline and cropped forebody strakes for  $M_\infty = 0.40, 0.60$ , and  $0.80$  and  $\beta = 0^\circ$  are given in figures 66 through 68. The results indicate that cropping the strake has a small effect on the yaw control effectiveness at  $M_\infty = 0.40$  (fig. 66). The decreases in the yawing moment and side force with the cropped strake at the higher angles of attack are caused by the reduced leading-edge length along which the strake vortex is formed. This causes a decrease in the strake vortex strength and a reduction in the circulation of opposite sense induced about the forebody. The strake cropping has a diminished effect on the yaw control effectiveness at  $M_\infty = 0.60$  (fig. 67) and  $M_\infty = 0.80$  (fig. 68). These results are analogous to the effect of small changes to the LEX exposed area on the lift of fighter aircraft at subsonic and transonic speeds (refs. 23 and 24). The rolling-moment characteristics are essentially unchanged at all Mach numbers. Both the baseline and cropped forebody strakes cause small, coupled rolling moments compared with the aileron rolling moment shown in figure 32.

Yawing-moment, side-force, and rolling-moment coefficient variations with sideslip for the baseline and cropped strakes at  $M_\infty = 0.60$  and  $\alpha = 30^\circ, 40^\circ$ , and  $50^\circ$  are shown in figures 69 through 71. The lateral-directional characteristics are relatively insensitive to cropping the strake at  $\alpha = 30^\circ$  and  $40^\circ$  (figs. 69 and 70). However, the yawing-moment variation with sideslip is more nonlinear with the cropped strake at  $\alpha = 50^\circ$  (fig. 71). Analysis of the LVS videotapes for the cropped strake shows that the forebody and LEX vortices are prone to decoupling at small sideslip angles. This effect is attributed to the reduced strake area and causes the discontinuities in the yawing-moment curve at  $\beta = -2^\circ$  and  $4^\circ$  (fig. 71(a)).

The lateral-directional characteristics in sideslip at  $M_\infty = 0.80$  and  $\alpha = 30^\circ$  and  $40^\circ$  for the baseline and cropped strakes are given in figures 72 and 73. The principal effect of cropping the strake is to slightly reduce the yawing moment at negative sideslip angles (nose right), where the strake is on the windward side. This trend is also associated with the smaller strake size. The LVS flow visualizations indi-

cate that the character of the vortex-dominated flow field about the forebody, LEX's, and wings in sideslip is insensitive to the strake planform at  $M_\infty = 0.80$ .

**Forebody surface static pressure distributions.** Figures 74 through 79 present the forebody surface pressures for the baseline and cropped strakes for  $M_\infty = 0.40, 0.60$ , and  $0.80$  and  $\alpha = 40^\circ$  and  $50^\circ$ . Cropping the strake generally promotes slightly higher suction pressure levels on the strake-deployed side of the forebody and slightly lower suction pressure levels on the side opposite the strake-off side. The induced effect of the vortex shed from the cropped strake is smaller because of the reduced strake area. This effect is consistent with the small decreases in yawing moment and side force caused by the cropped strake compared with the baseline strake at  $M_\infty = 0.40$  to  $0.80$  (figs. 66–68). The nominal differences in the overall pressure distributions at  $M_\infty = 0.40$  to  $0.80$  confirm the insensitivity of the strake yaw control flow mechanism to the strake cropping at subsonic and transonic speeds.

## Concluding Remarks

Wind tunnel investigations have been conducted of a forebody strake yaw control device applied to 0.06-scale models of the F/A-18 aircraft. The effects of the Mach number and strake planform on the strake yaw control effectiveness and the strake-vortex-induced flow-field have been determined. Off-surface and on-surface flow patterns, six component forces and moments, and forebody and wing leading-edge extension (LEX) surface static pressure distributions have shown that the strake generates a strong vortex that modulates the flow field along the entire forebody. The strake vortex induces a circulation of opposite sense about the forebody that delays primary boundary-layer separation and promotes higher attached flow suction pressures along the strake-off side of the forebody. The differential suction pressures induced on the forebody, acting through the long forebody moment arm, produce large yawing moments at high angles of attack. The strake has been shown to produce small coupled pitching moments and rolling moments and acts essentially as a decoupled yaw control device at angles of attack of  $25^\circ$  and higher. The present results have identified a forebody vortex–LEX vortex decoupling mechanism at angles of attack beyond maximum lift caused by the development of a wake-like flow shed from the LEX. The forebody–LEX flow-field decoupling limits the maximum yawing moment caused by the strake. The character of the strake-vortex-induced flow field is similar through the range of Mach number from 0.20 to 0.90. The strake

yaw control diminishes with increasing Mach number, however, because of diminished strake vortex strength and corresponding reduction in the induced circulation about the forebody. Despite this trend, the strake yaw control exceeds that of conventional rudders at all Mach numbers and angles of attack greater than about  $30^\circ$ .

Comparisons of a baseline, gothic-shaped strake (leading-edge sweep continuously increasing along the strake length) and a derivative cropped strake have shown that the strake cropping has a small effect on the yaw control effectiveness at low subsonic speeds. This small effect is caused by the reduced area, or shorter vortex-generating length, on the cropped strake. The effect of strake cropping on yaw control is nearly transparent at higher subsonic and transonic speeds.

NASA Langley Research Center  
Hampton, VA 23681-0001  
June 28, 1993

## References

1. Gilbert, William P.; and Gatlin, Donald H.: Review of the NASA High-Alpha Technology Program. *High-Angle-of-Attack Technology*, Volume I, Joseph R. Chambers, William P. Gilbert, and Luat T. Nguyen, eds., NASA CP-3149, Part 1, 1992, pp. 23-59.
2. Regenie, Victoria; Gatlin, Donald; Kempel, Robert; and Matheny, Neil: *The F-18 High Alpha Research Vehicle: A High Angle-of-Attack Testbed Aircraft*. NASA TM-104253, 1992.
3. Murri, Daniel G.; and Rao, Dhanvada, M.: Exploratory Studies of Actuated Forebody Strakes for Yaw Control at High Angles of Attack. AIAA-87-2557, Aug. 1987.
4. Murri, Daniel G.; Biedron, Robert T.; Erickson, Gary E.; Jordan, Frank L., Jr.; and Hoffer, Keith D.: Development of Actuated Forebody Strake Controls for the F-18 High Alpha Research Vehicle. *High-Angle-of-Attack Technology*, Volume I, Joseph R. Chambers, William P. Gilbert, and Luat T. Nguyen, eds., NASA CP-3149, Part 1, 1992, pp. 335-380.
5. Murri, Daniel G.; Shah, Gautam H.; DiCarlo, Daniel J.; Lord, Mark T.; and Strickland, Mark E.: Status of Ground and Flight Research on Actuated Forebody Strake Controls. *High-Angle-of-Attack Projects and Technology Conference*, Volume 3, Neil W. Matheny, compiler, NASA CP-3137, 1992, pp. 261-282.
6. Ghaffari, Farhad; Luckring, James M.; Thomas, James L.; and Bates, Brent L.: Navier-Stokes Solutions About the F/A-18 Forebody-Leading-Edge Extension Configuration. *J. Aircr.*, vol. 27, Sept. 1990, pp. 737-748.
7. McGregor, I.: The Vapour-Screen Method of Flow Visualization. *J. Fluid Mech.*, vol. 11, pt. 4, Dec. 1961, pp. 481-511.
8. Banks, Daniel W.: Wind-Tunnel Investigation of the Forebody Aerodynamics of a Vortex-Lift Fighter Configuration at High Angles of Attack. *Advanced Aerospace Aerodynamics*, SP-757, Soc. of Automotive Engineers, Inc., Oct. 1988, pp. 101-123. (Available as SAE 881419.)
9. ASED Staff: *Transonic Wind-Tunnel Facility at the Naval Ship Research and Development Center*. ASED Rep. 332, David W. Taylor Naval Ship Research and Development Center, June 1975. (Available from DTIC as AD A014 927.)
10. Fox, Charles H., Jr.; and Huffman, Jarrett K.: *Calibration and Test Capabilities of the Langley 7- by 10-Foot High Speed Tunnel*. NASA TM X-74027, 1977.
11. Erickson, Gary E.: *Wind Tunnel Investigation of Vortex Flows on F/A-18 Configuration at Subsonic Through Transonic Speeds*. NASA TP-3111, 1991.
12. Erickson, Gary E.; and Inenaga, Andrew S.: Fiber Optic-Based Laser Vapor Screen Flow Visualization Systems for Aerodynamics Research in Larger-Scale Subsonic and Transonic Wind Tunnels. Paper presented at the 6th International Flow Visualization Symposium (Yokohama, Japan), Oct. 4-9, 1992.
13. Skow, A. M.; and Erickson, G. E.: Modern Fighter Aircraft Design for High-Angle-of-Attack Maneuvering. *High Angle-of-Attack Aerodynamics*, AGARD-LS-121, Dec. 1982, pp. 4-1-4-59.
14. Fisher, David F.; Del Frate, John H.; and Richwine, David M.: *In-Flight Flow Visualization Characteristics of the NASA F-18 High Alpha Research Vehicle at High Angles of Attack*. NASA TM-4193, 1990.
15. Biedron, Robert T.; and Thomas, James L.: Navier-Stokes Computations for an F-18 Forebody With Actuated Control Strake. *High-Angle-of-Attack Technology*, Volume I, Joseph R. Chambers, William P. Gilbert, and Luat T. Nguyen, eds., NASA CP-3149, Part 1, 1992, pp. 481-506.
16. Küchemann, D.: *The Aerodynamic Design of Aircraft*. Pergamon Press Inc., c.1978, pp. 368-369.
17. Vorropoulos, G.; and Wendt, J. F.: Laser Velocimetry Study of Compressibility Effects on the Flow Field of a Delta Wing. *Aerodynamics of Vortical Type Flows in Three Dimensions*, AGARD-CP-342, July 1983, pp. 9-1-9-13. (Available from DTIC as AD A135 157.)
18. Erickson, Gary E.; and Rogers, Lawrence W.: *Experimental Study of the Vortex Flow Behavior on a Generic Fighter Wing at Subsonic and Transonic Speeds*. NASA TM-89446, 1987.

19. Erickson, G. E.: *Vortex Flow Correlation*. AFWAL-TR-80-3143, U.S. Air Force, Jan. 1981. (Available from DTIC as AD A108 725.)
20. Hall, M. G.: Vortex Breakdown. *Annual Review of Fluid Mechanics*, Volume 4, M. Van Dyke, W. G. Vincenti, and J. V. Wehausen, eds., Annual Reviews, Inc., 1972, pp. 195–218.
21. Erickson, G. E.: Effects of Spanwise Blowing on the Aerodynamic Characteristics of the F-5E. AIAA-79-0118, Jan. 1979.
22. Erickson, Gary E.: *Wind Tunnel Investigation of the Interaction and Breakdown Characteristics of Slender-Wing Vortices at Subsonic, Transonic, and Supersonic Speeds*. NASA TP-3114, 1991.
23. Headley, Jack W.: *Analysis of Wind Tunnel Data Pertaining to High Angle of Attack Aerodynamics, Volume I: Technical Discussion and Analysis of Results*. AFFDL-TR-78-94-VOL-1, U.S. Air Force, July 1978. (Available from DTIC as AD A069 646.)
24. Headley, Jack W.: *Analysis of Wind Tunnel Data Pertaining to High Angle of Attack Aerodynamics, Volume II: Data Base*. AFFDL-TR-78-94-VOL-2, U.S. Air Force, July 1978. (Available from DTIC as AD A069 647.)

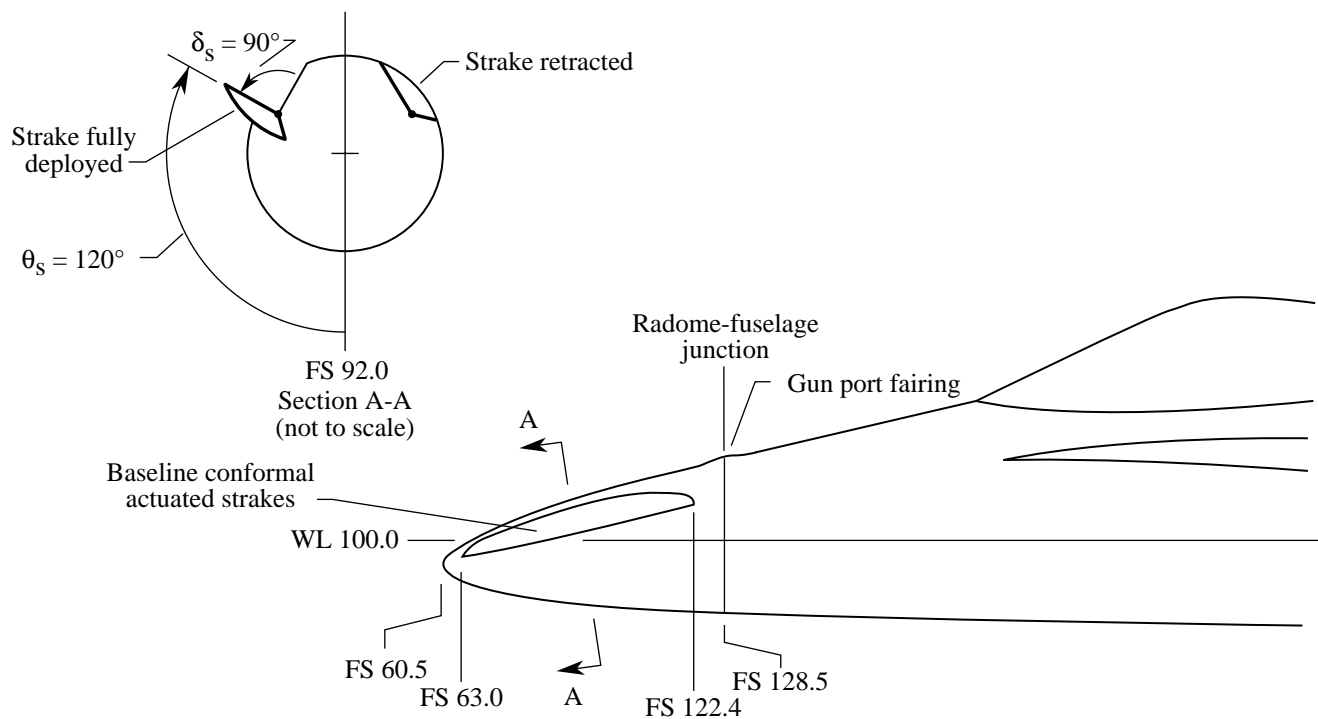


Figure 1. Conformal actuated forebody strake concept. Dimensions are in inches full scale.

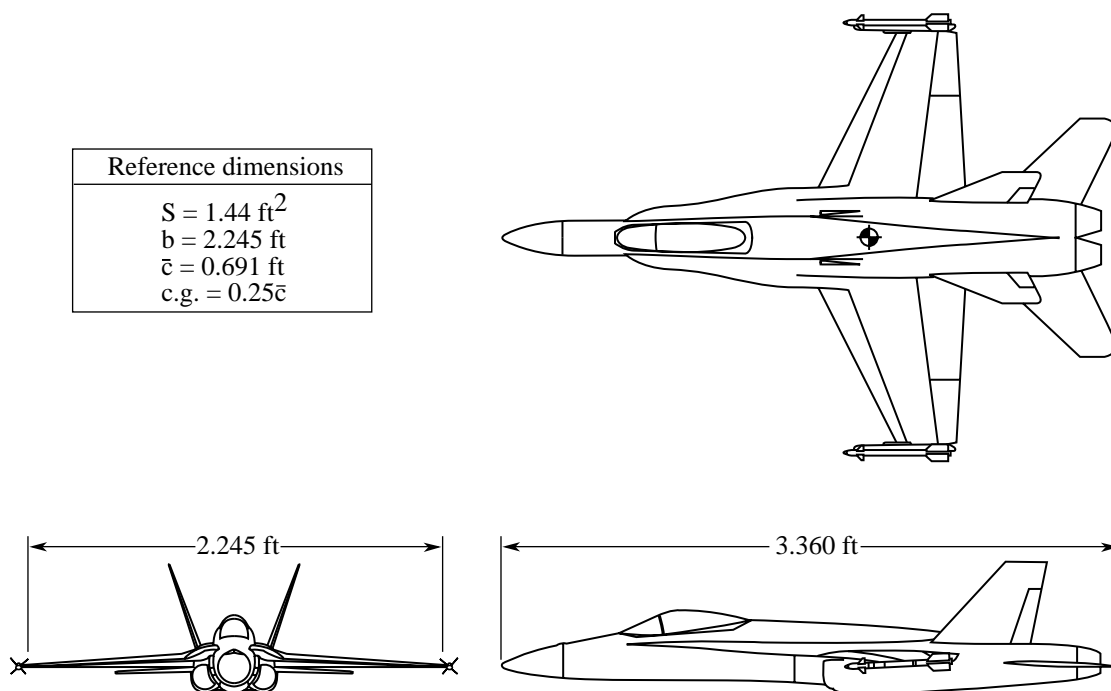


Figure 2. Three-view sketch of 0.06-scale F/A-18 model.

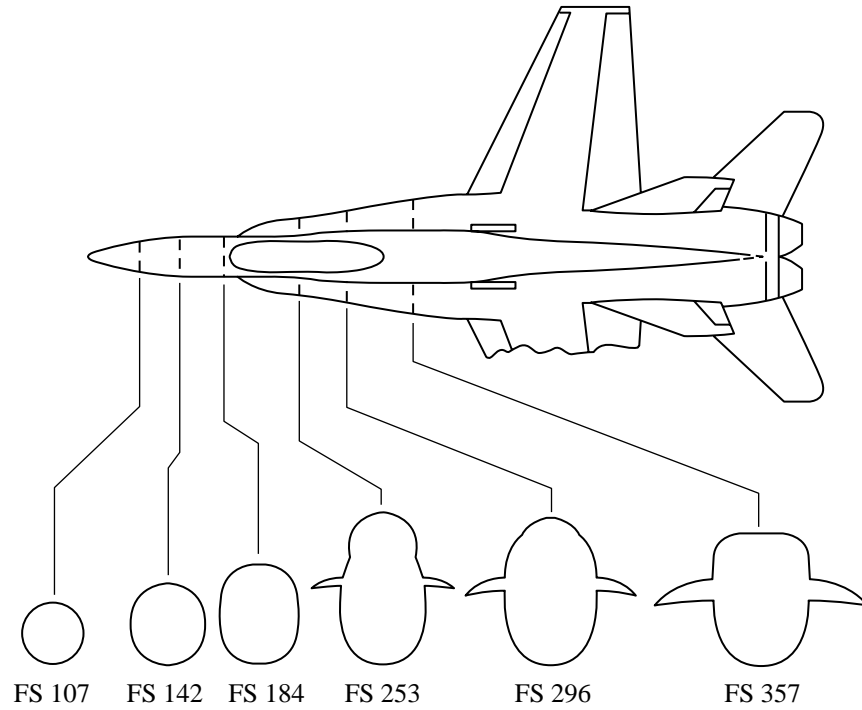


Figure 3. Forebody and LEX surface static pressure measurement stations. Dimensions are in inches full scale.

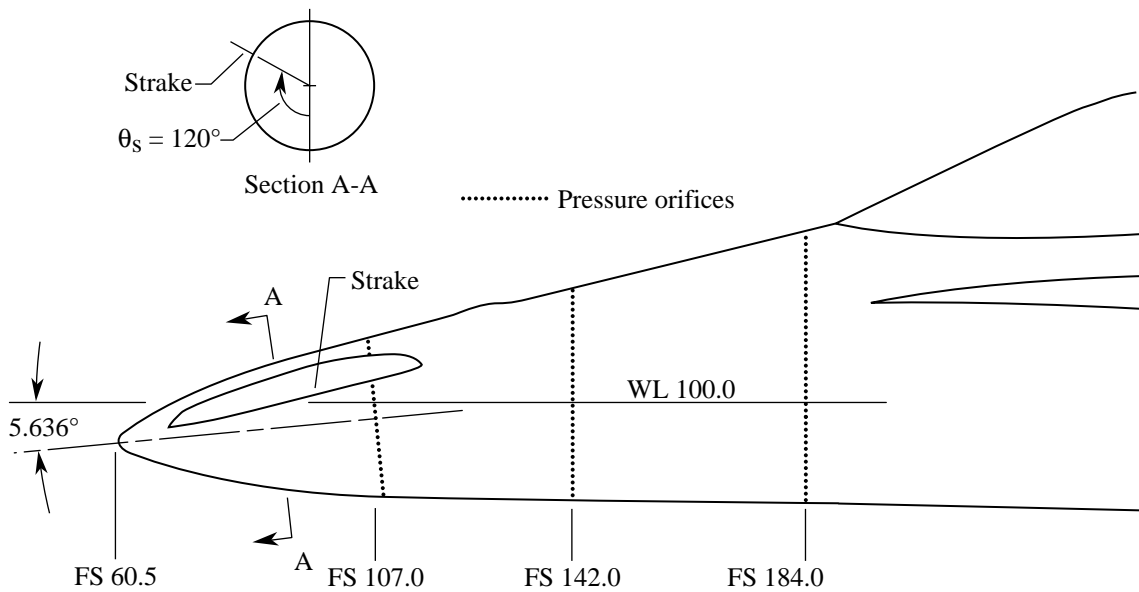
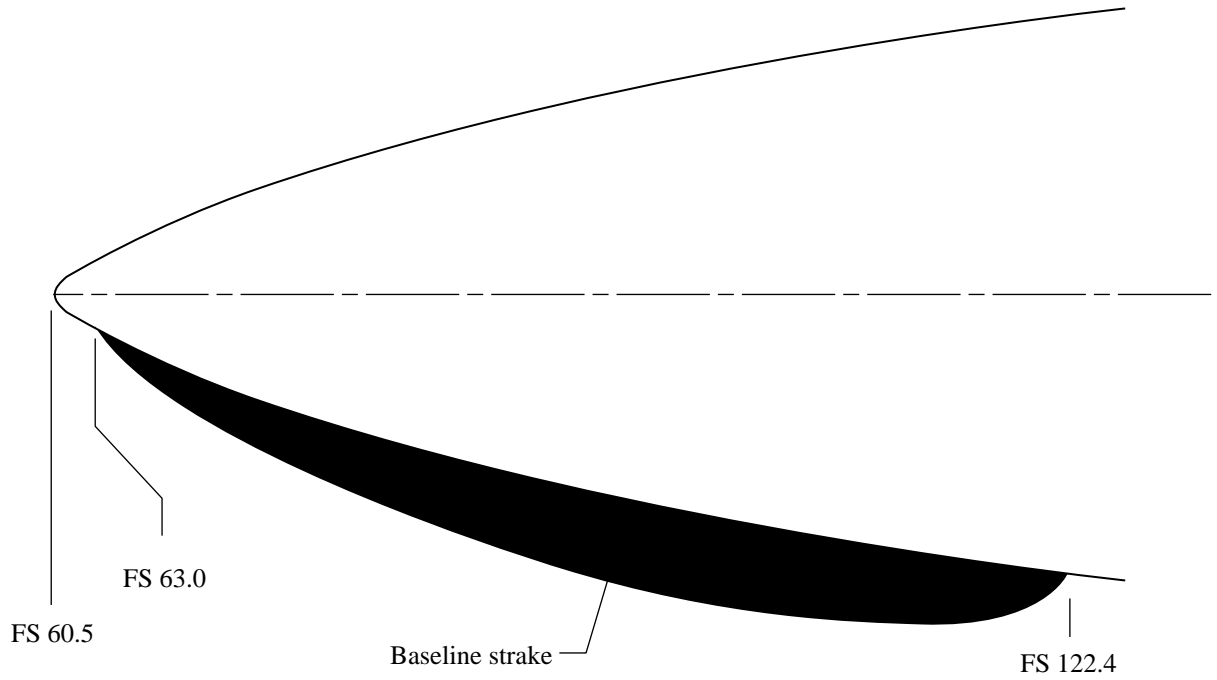
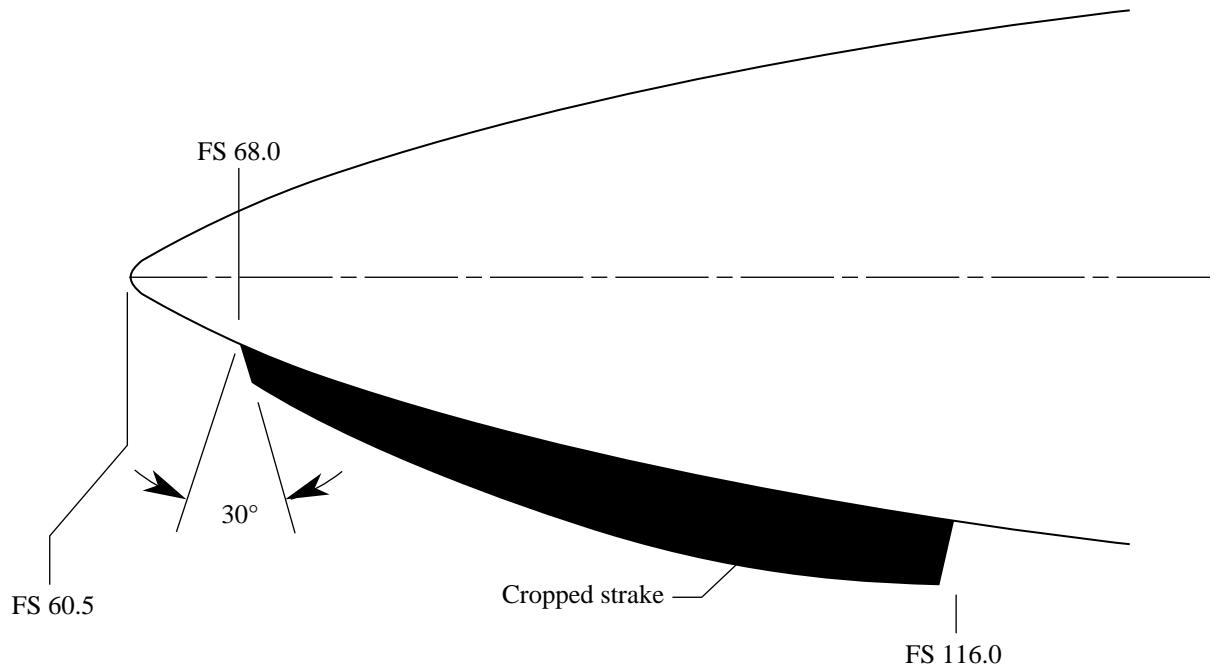


Figure 4. Sketch of location and orientation of forebody strake. Dimensions are in inches full scale.



(a) Baseline strake.



(b) Cropped strake.

Figure 5. Planviews of baseline and cropped forebody strakes. Dimensions are in inches full scale.

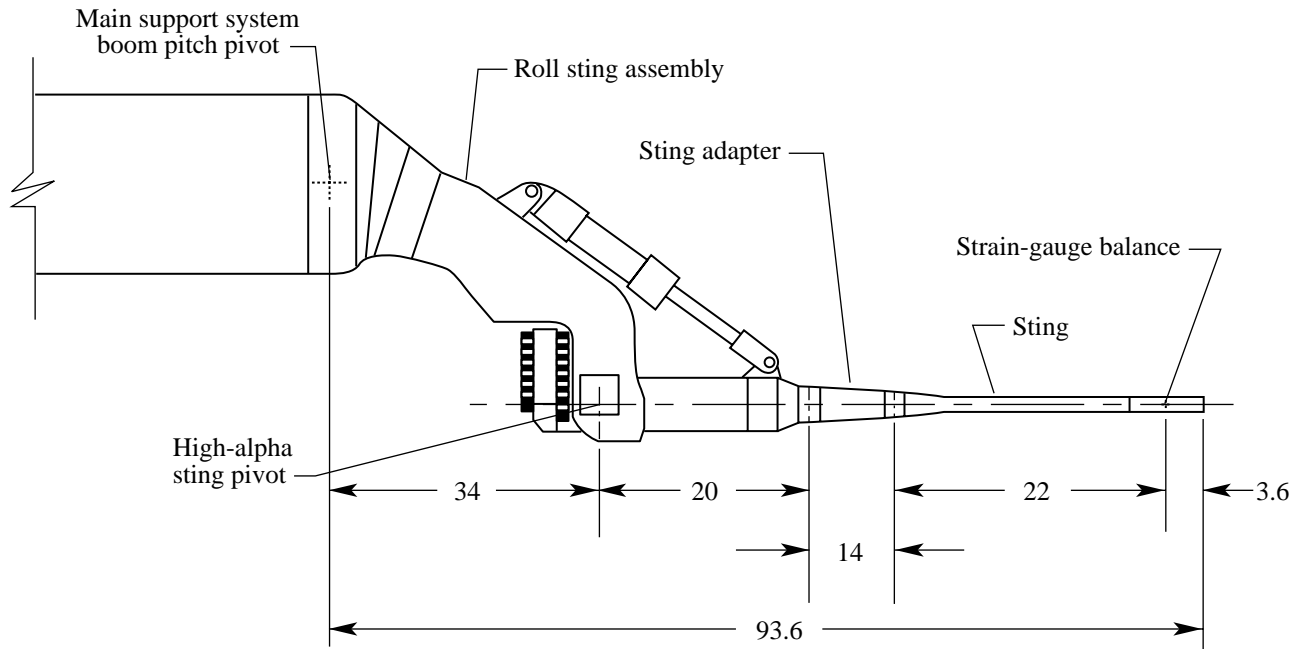


Figure 6. Details of high-angle-of-attack support system in 7- by 10-Foot Transonic Tunnel at DTRC. Dimensions are in inches.

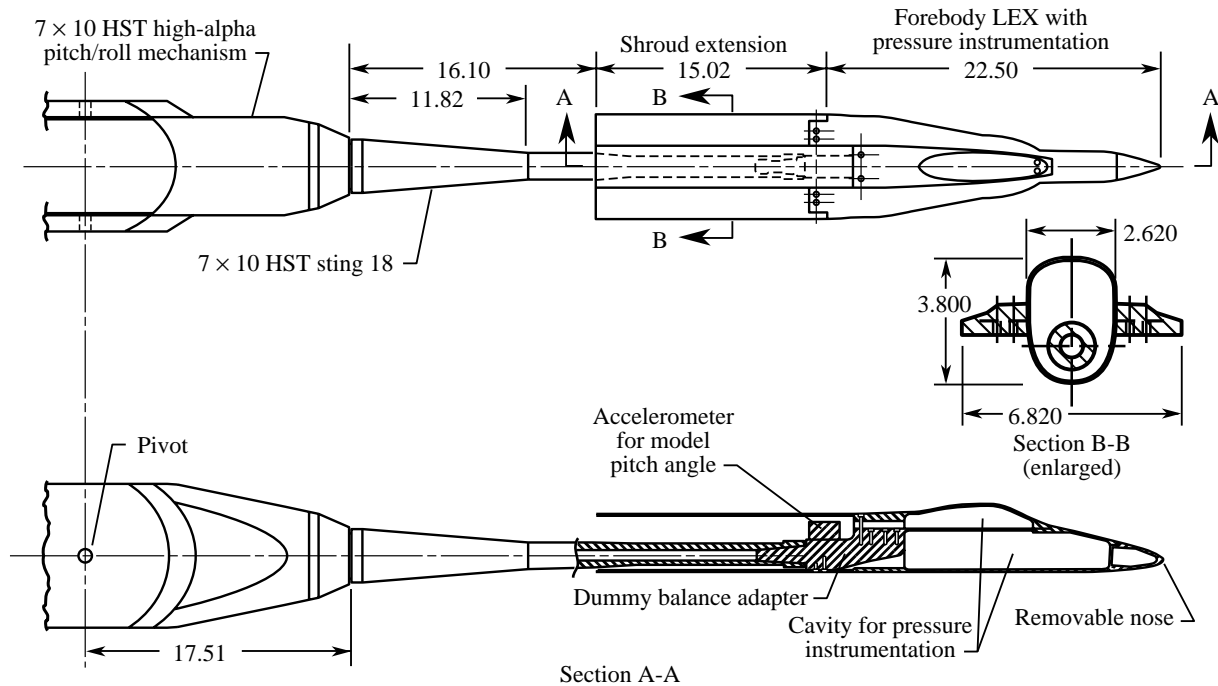
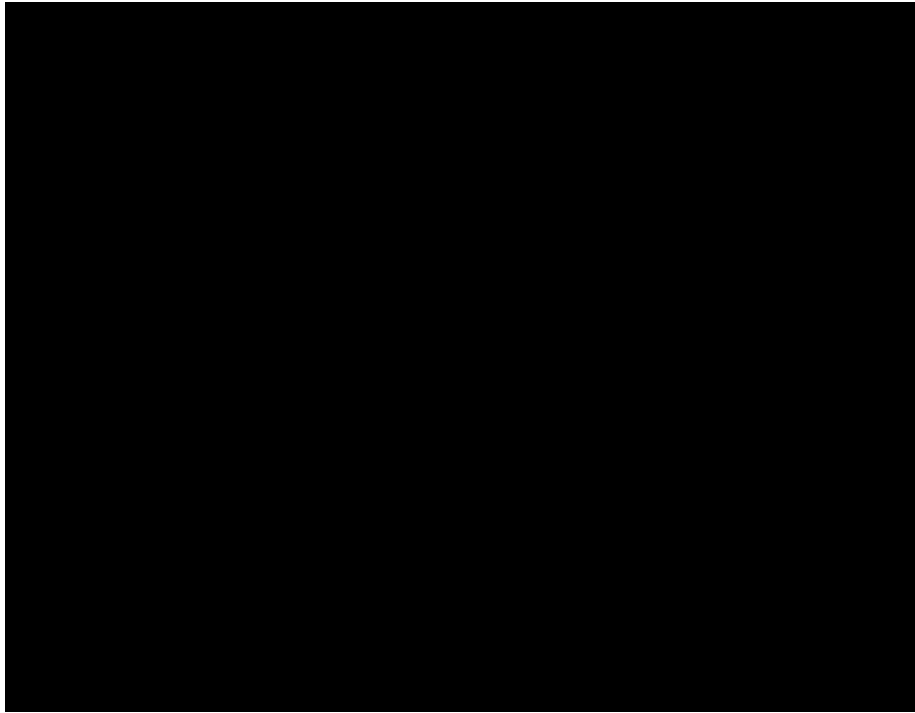
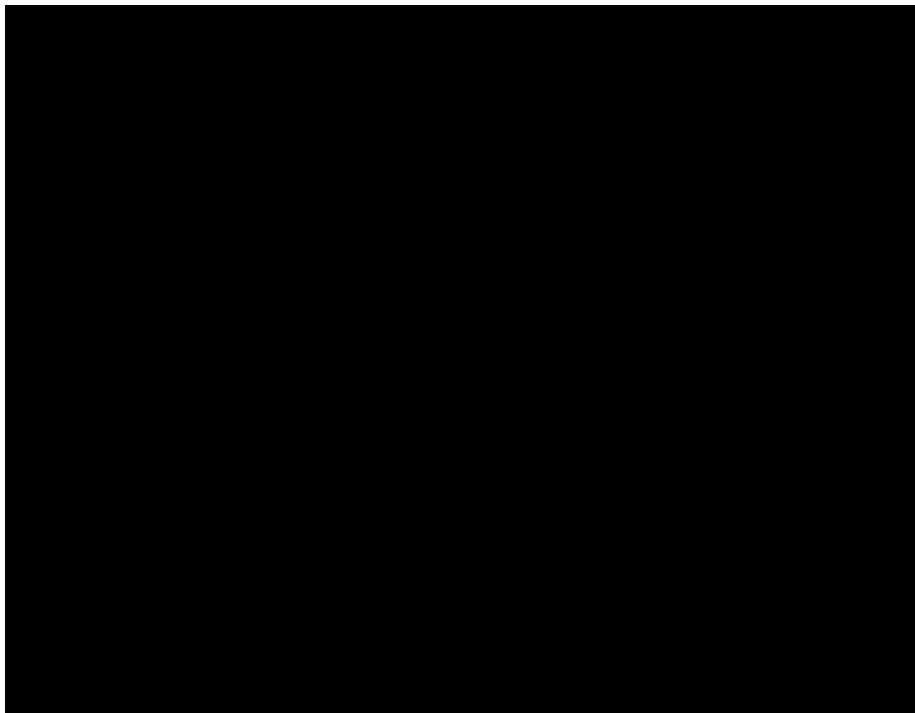


Figure 7. Details of 0.06-scale F/A-18 front end assembly with aft shroud. Dimensions are in inches model scale.

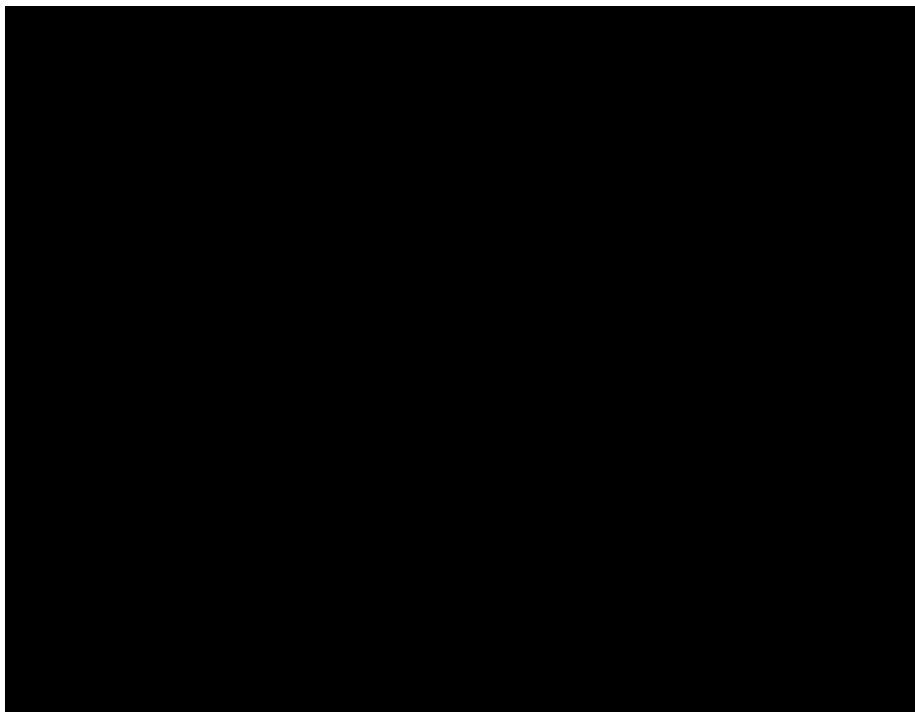


(a)  $\alpha = 20^\circ$ .

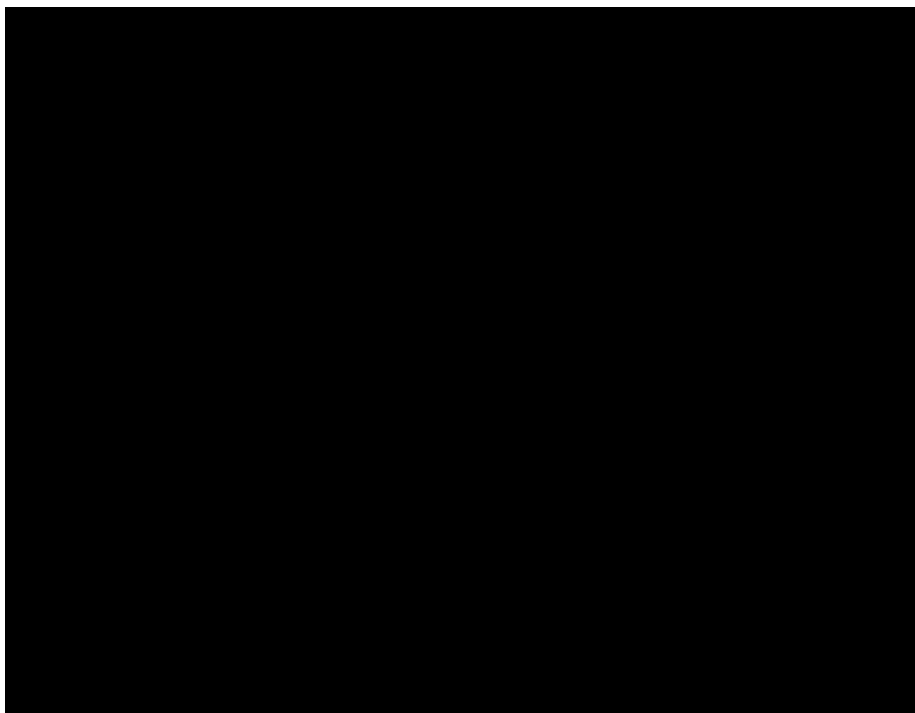


(b)  $\alpha = 25^\circ$ .

Figure 10. Vapor screen flow visualization at  $M_\infty = 0.40$  and  $\beta = 0^\circ$  with baseline strake on.

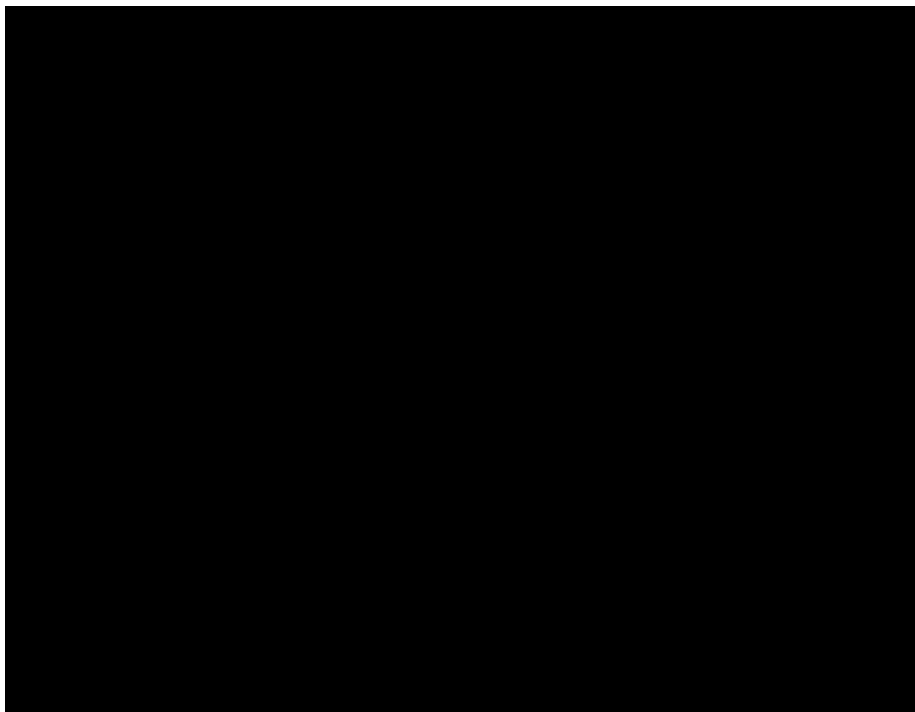


(c)  $\alpha = 25^\circ$  (close-up).

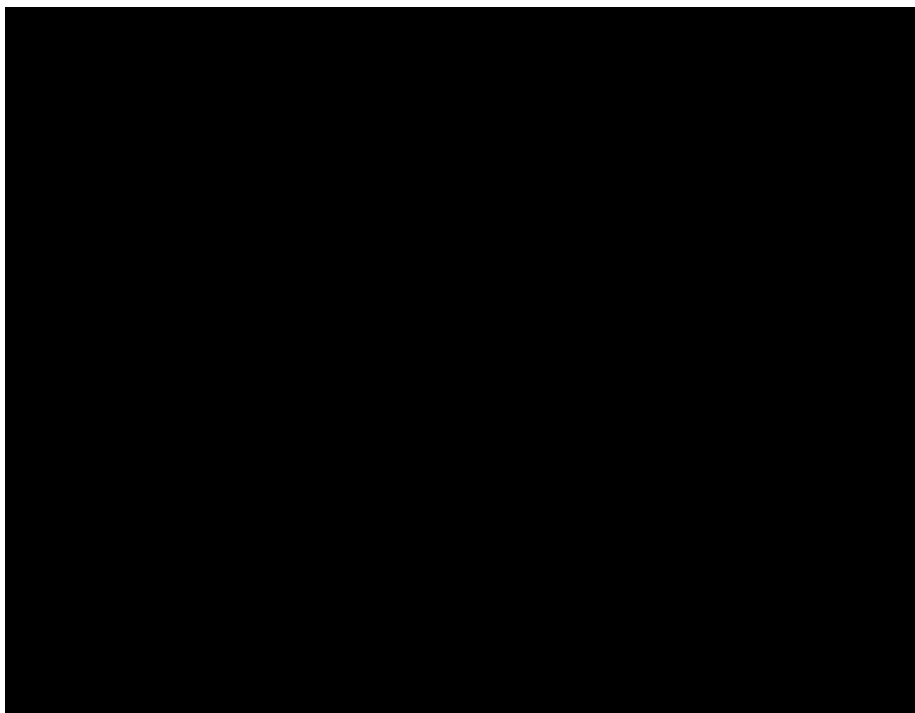


(d)  $\alpha = 30^\circ$ .

Figure 10. Continued.

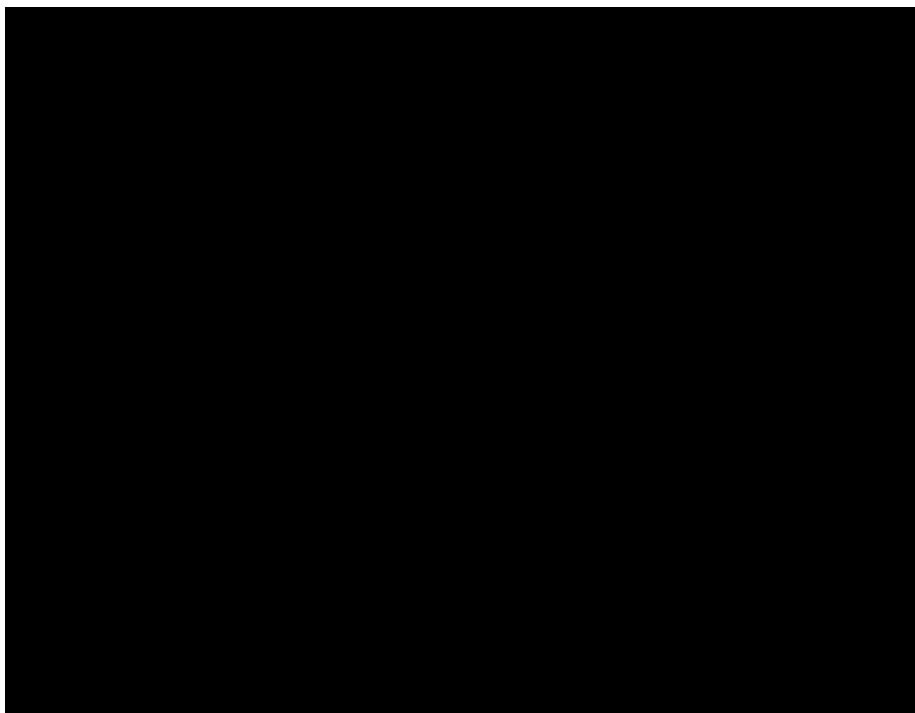


(e)  $\alpha = 35^\circ$ .

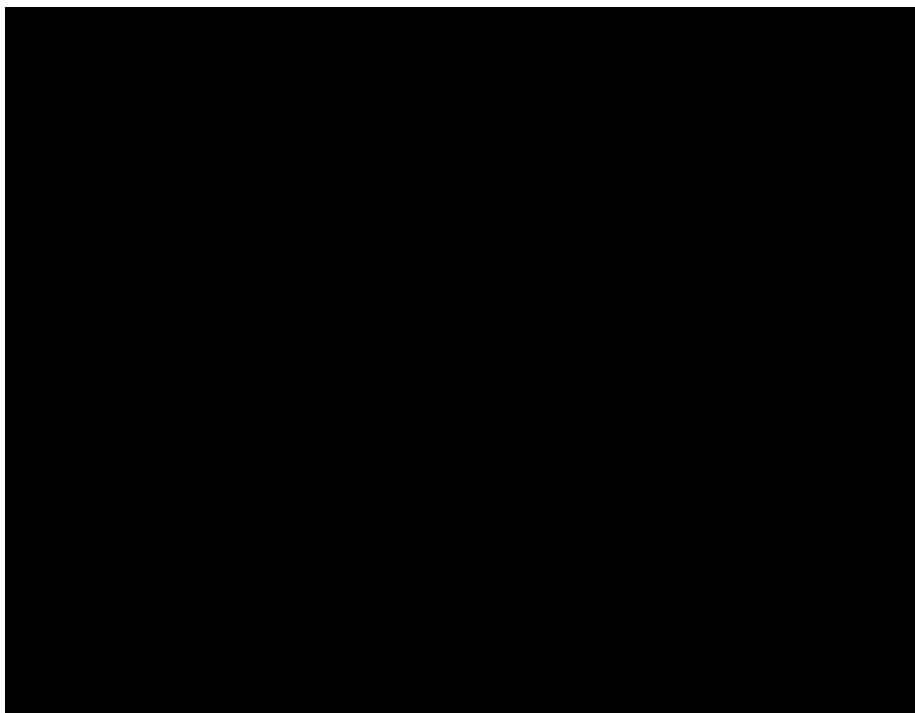


(f)  $\alpha = 40^\circ$ .

Figure 10. Concluded.

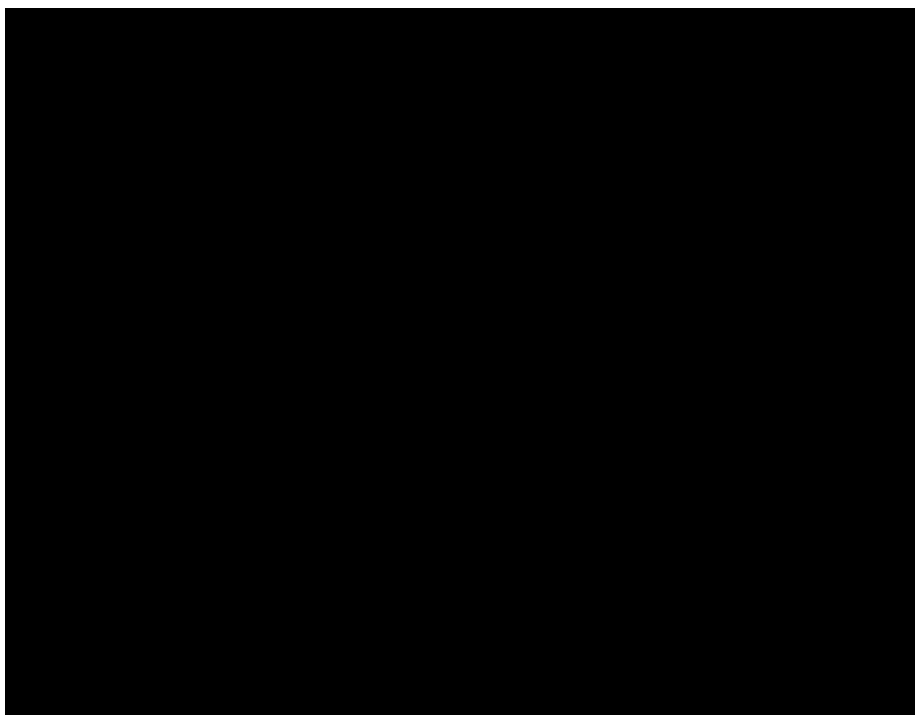


(a)  $\alpha = 25^\circ$ .



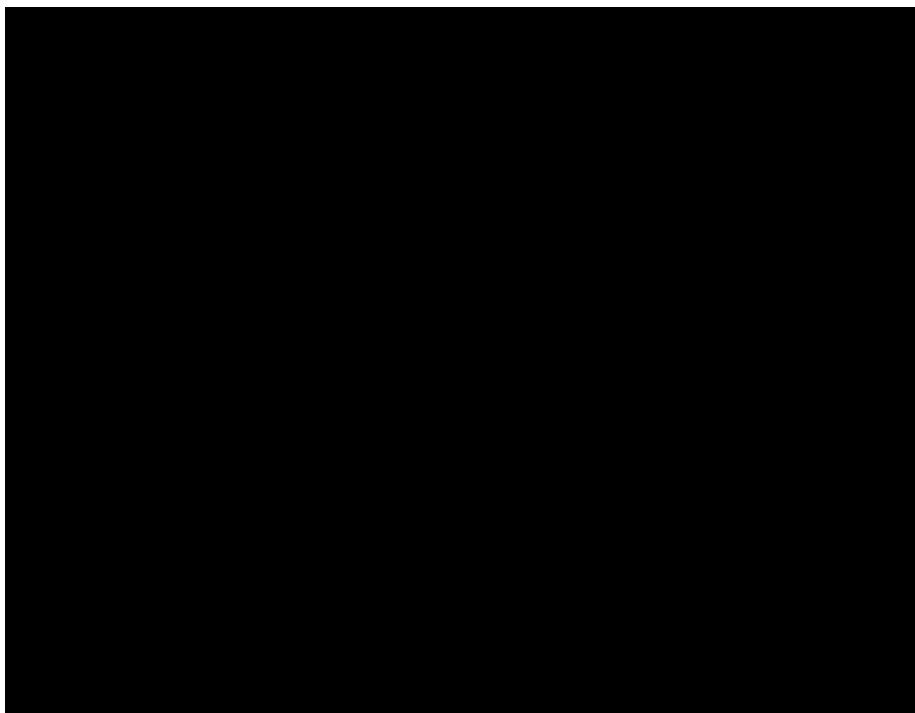
(b)  $\alpha = 30^\circ$ .

Figure 11. Vapor screen flow visualization at  $M_\infty = 0.40$  and  $\beta = 0^\circ$  with baseline strake on and light sheet near aft canopy region.

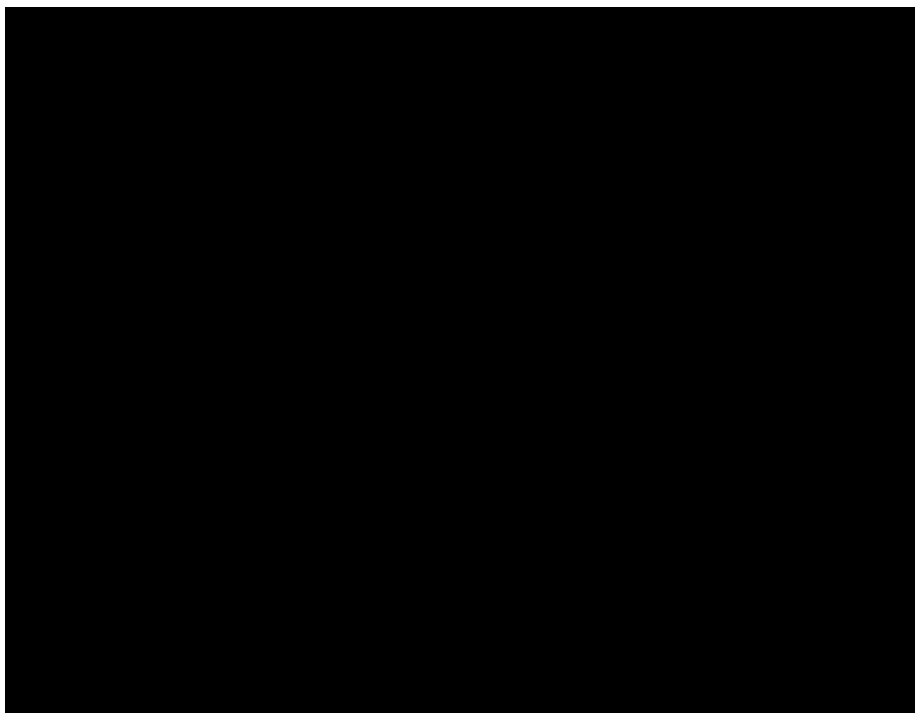


(c)  $\alpha = 35^\circ$ .

Figure 11. Concluded.

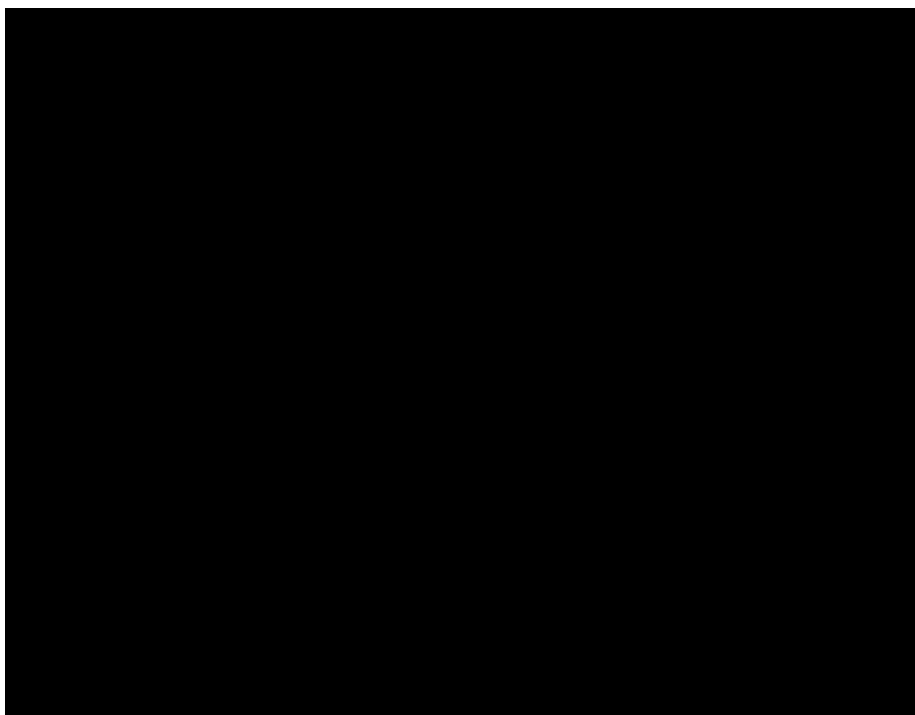


(a)  $\alpha = 25^\circ$ .



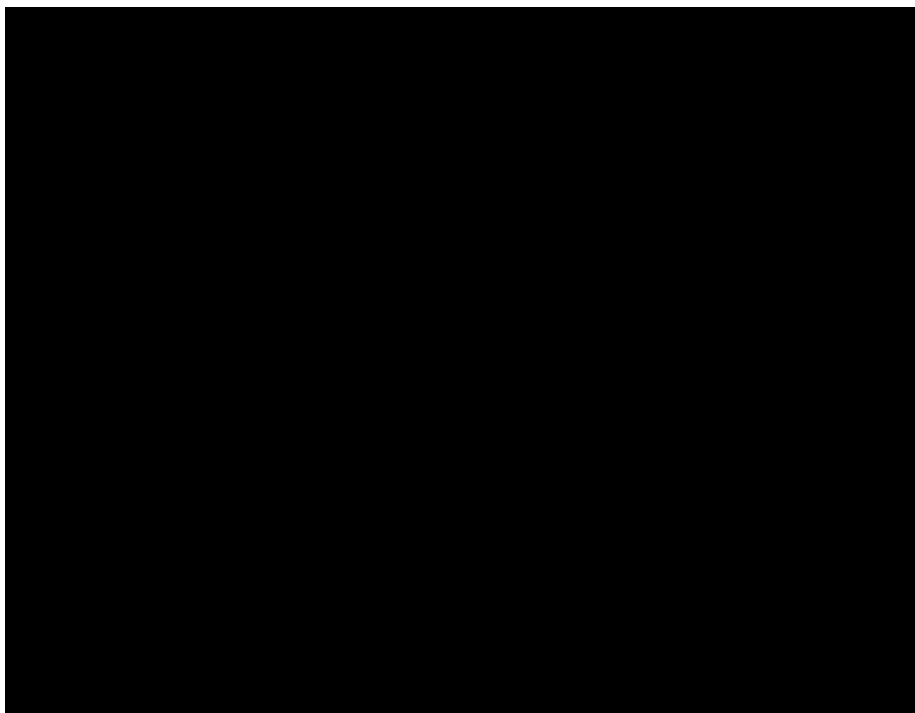
(b)  $\alpha = 30^\circ$ .

Figure 12. Vapor screen flow visualization at  $M_\infty = 0.40$  and  $\beta = 0^\circ$  with baseline strake on and light sheet near LEX-wing junction.

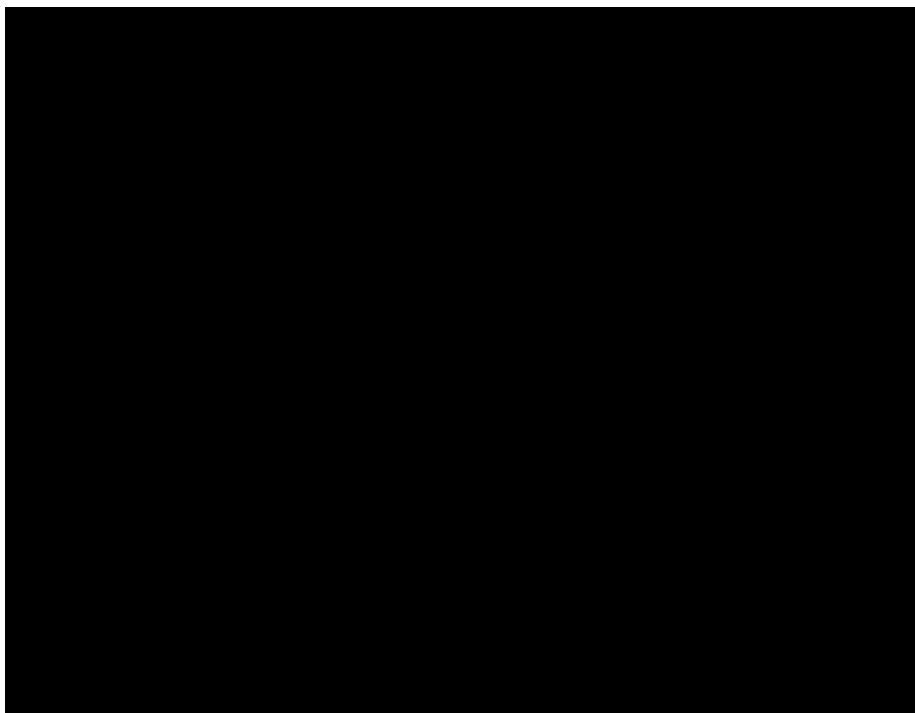


(c)  $\alpha = 35^\circ$ .

Figure 12. Concluded.

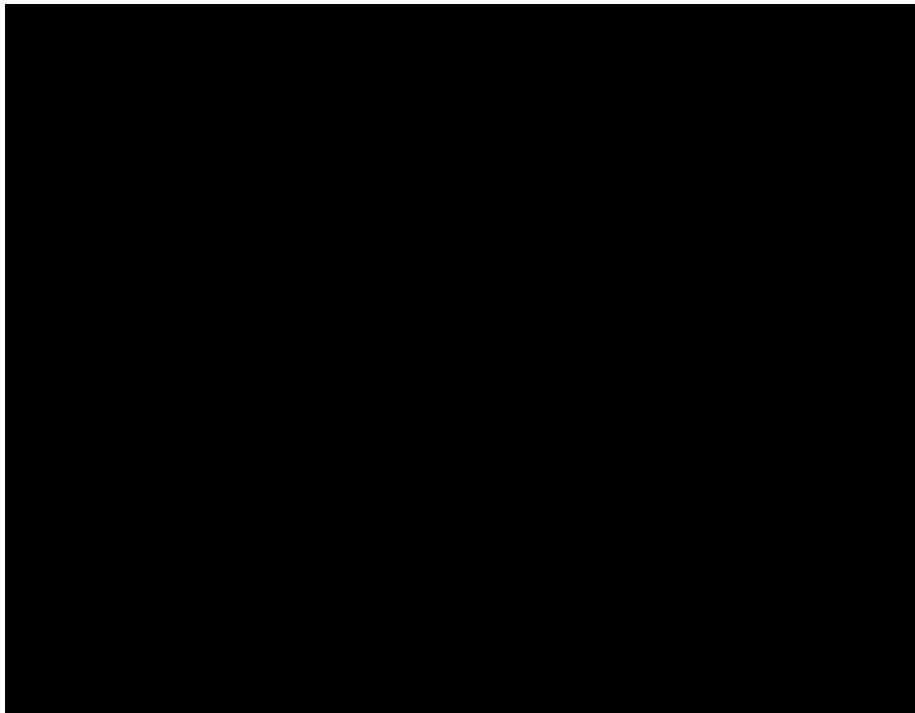


(a)  $\alpha = 25^\circ$ .



(b)  $\alpha = 30^\circ$ .

Figure 13. Vapor screen flow visualization at  $M_\infty = 0.40$  and  $\beta = 0^\circ$  with baseline strake on and light sheet near vertical tail apex.

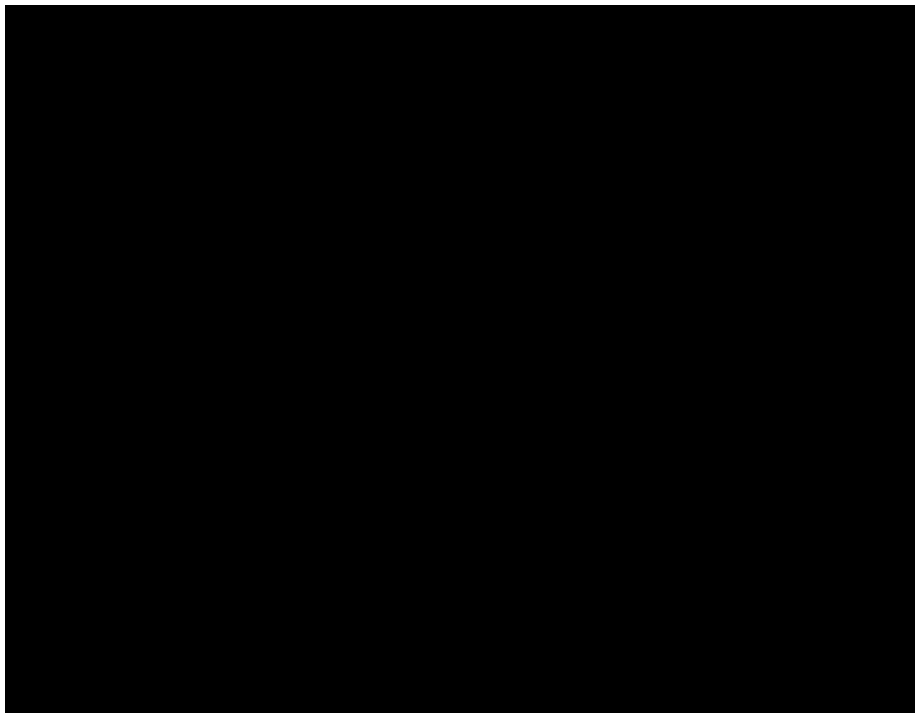


(c)  $\alpha = 35^\circ$ .

Figure 13. Concluded.

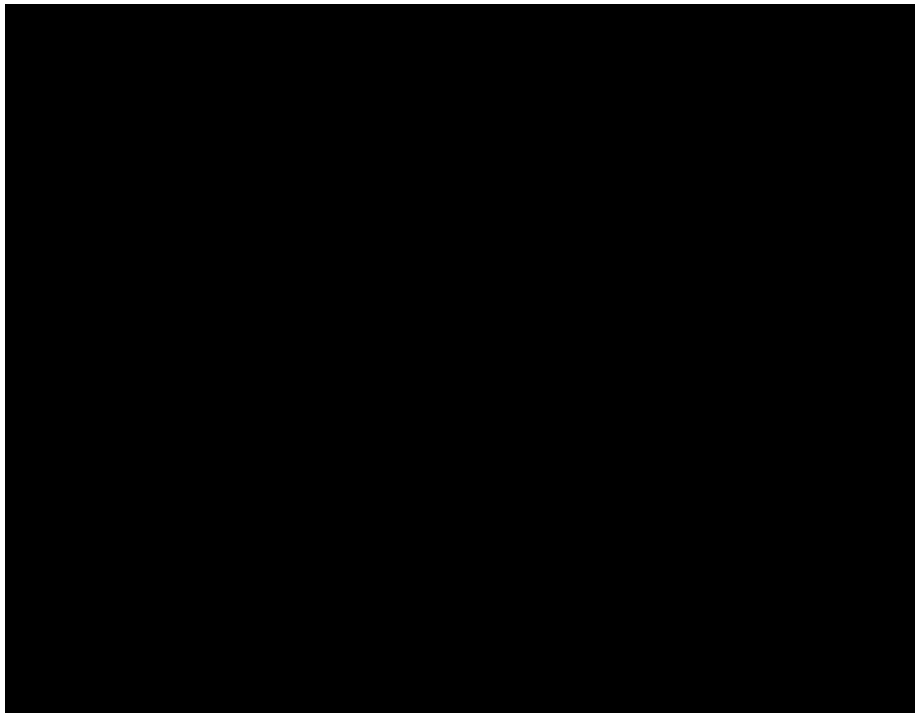


(a)  $\alpha = 20^\circ$ .

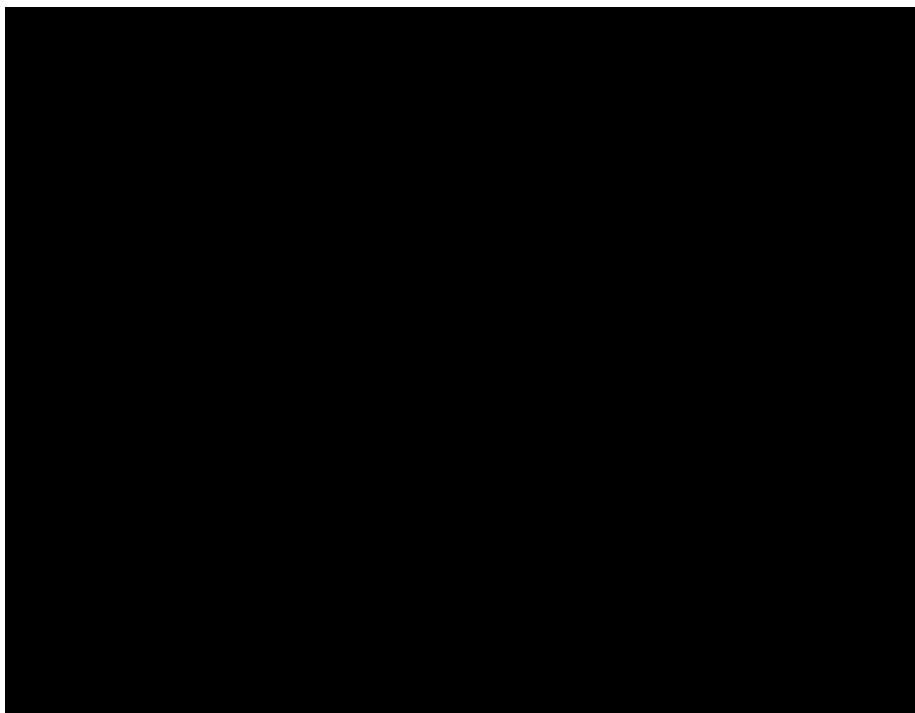


(b)  $\alpha = 25^\circ$ .

Figure 14. Vapor screen flow visualization at  $M_\infty = 0.80$  and  $\beta = 0^\circ$  with baseline strake on.

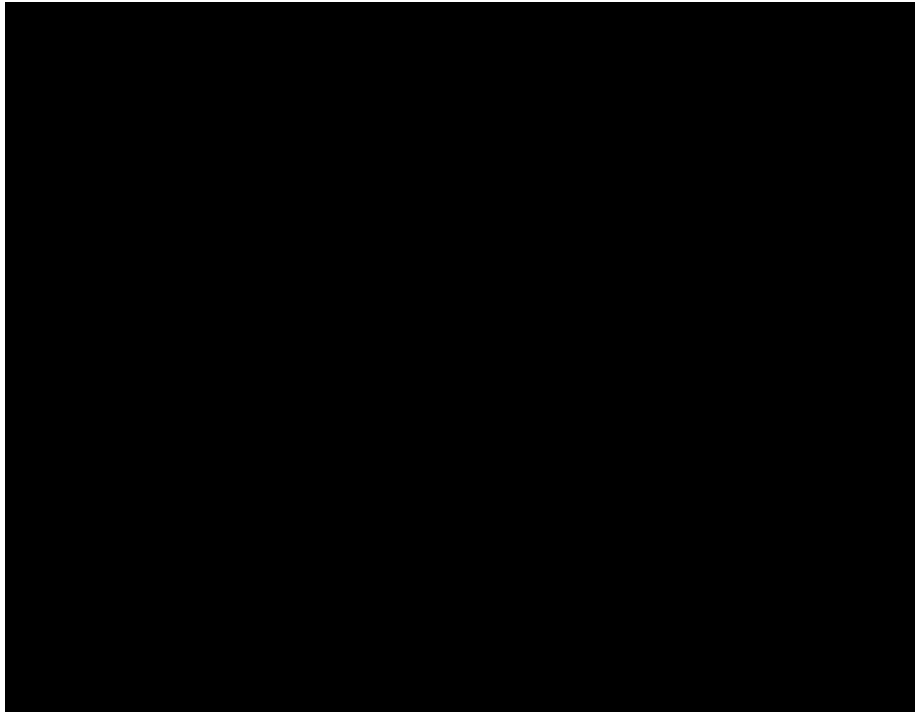


(c)  $\alpha = 30^\circ$ .

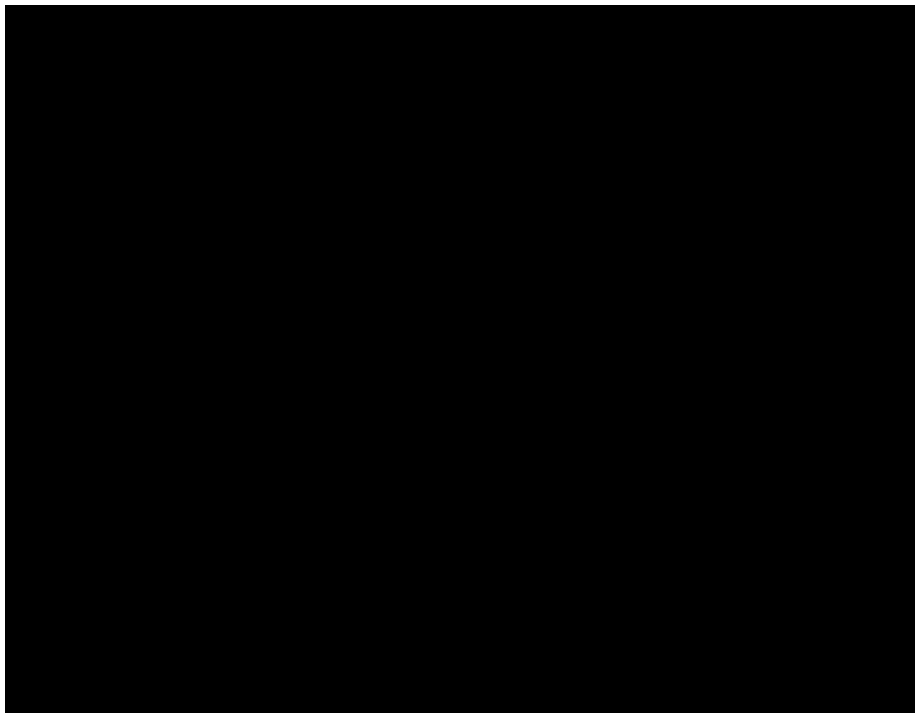


(d)  $\alpha = 35^\circ$ .

Figure 14. Concluded.

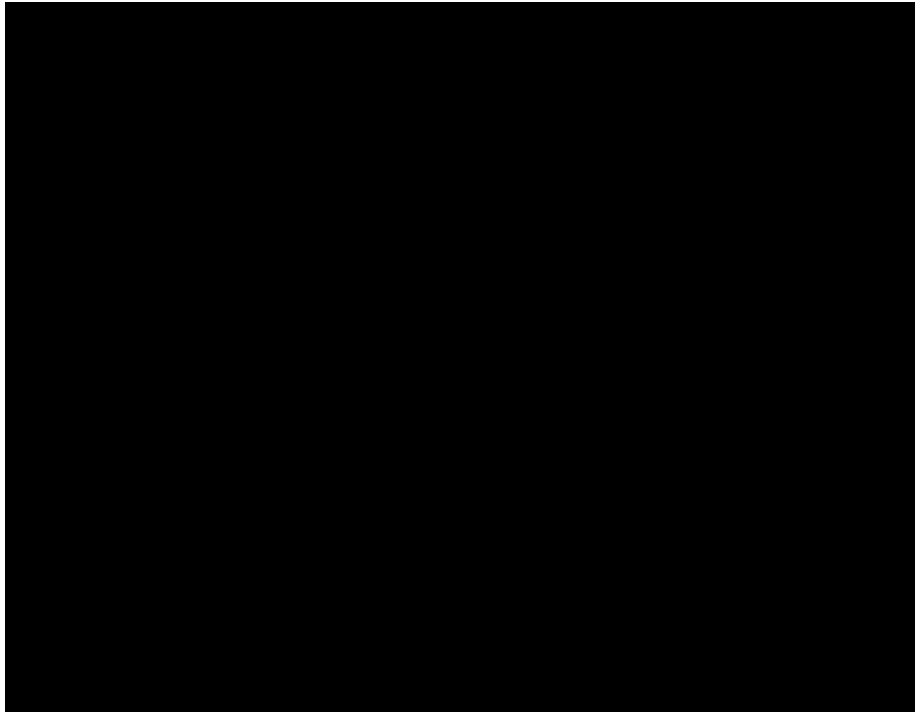


(a) Light sheet near wing mid-chord.

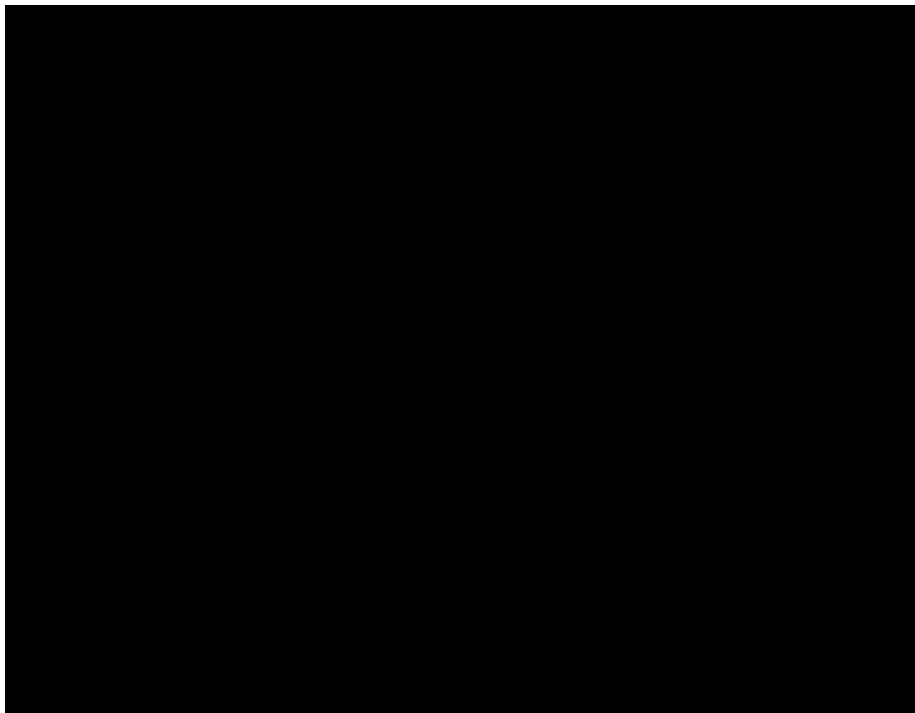


(b) Light sheet near model base.

Figure 15. Vapor screen flow visualization at  $M_\infty = 0.80$ ,  $\alpha = 20^\circ$ , and  $\beta = 0^\circ$  with baseline strake on.

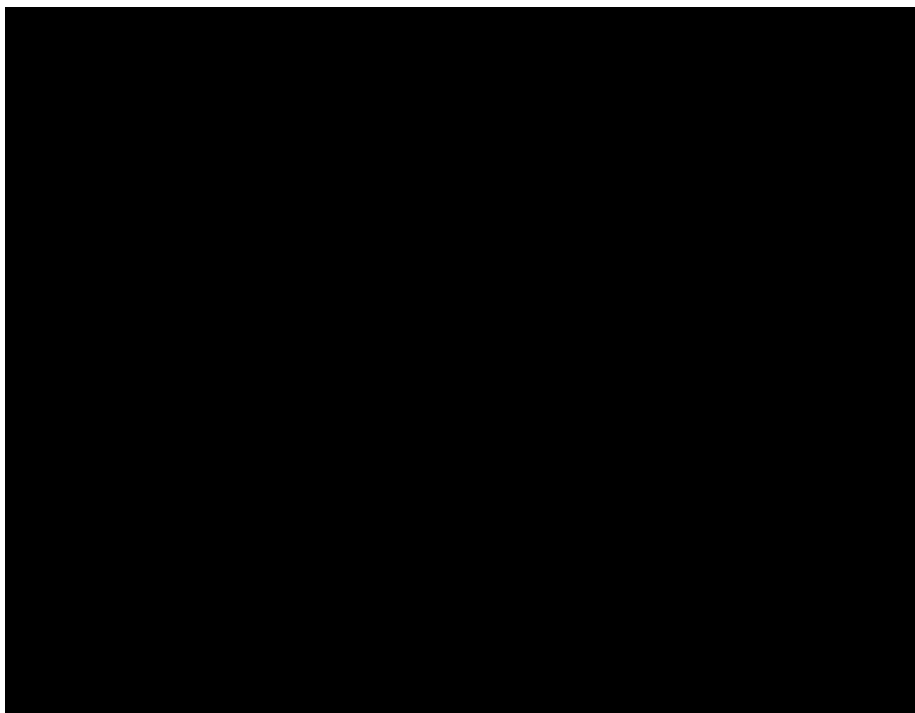


(a) Light sheet near wing mid-chord.

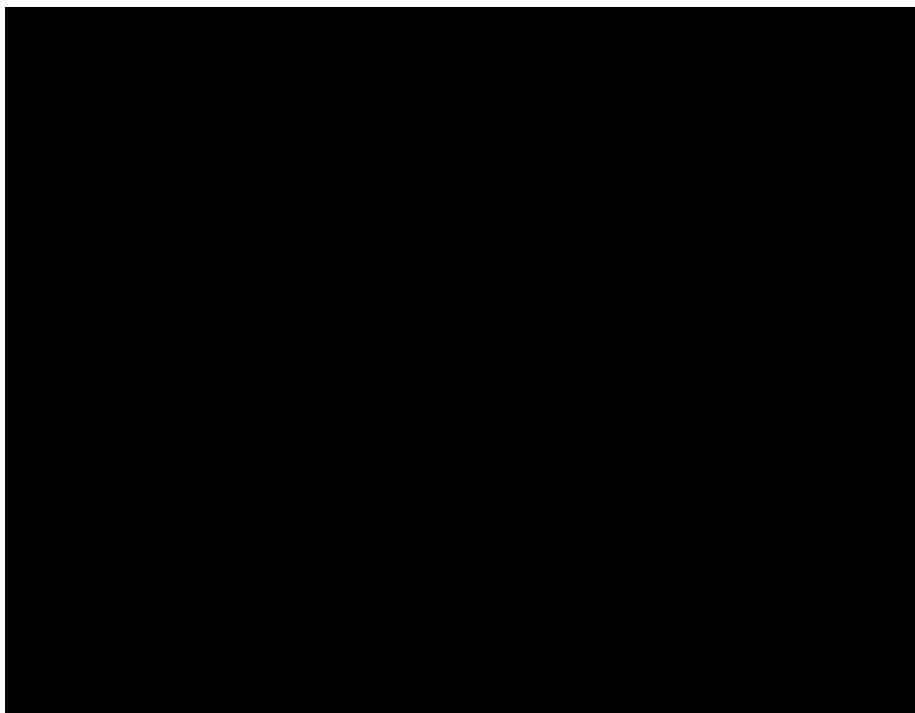


(b) Light sheet near model base.

Figure 16. Vapor screen flow visualization at  $M_\infty = 0.80$ ,  $\alpha = 25^\circ$ , and  $\beta = 0^\circ$  with baseline strake on.

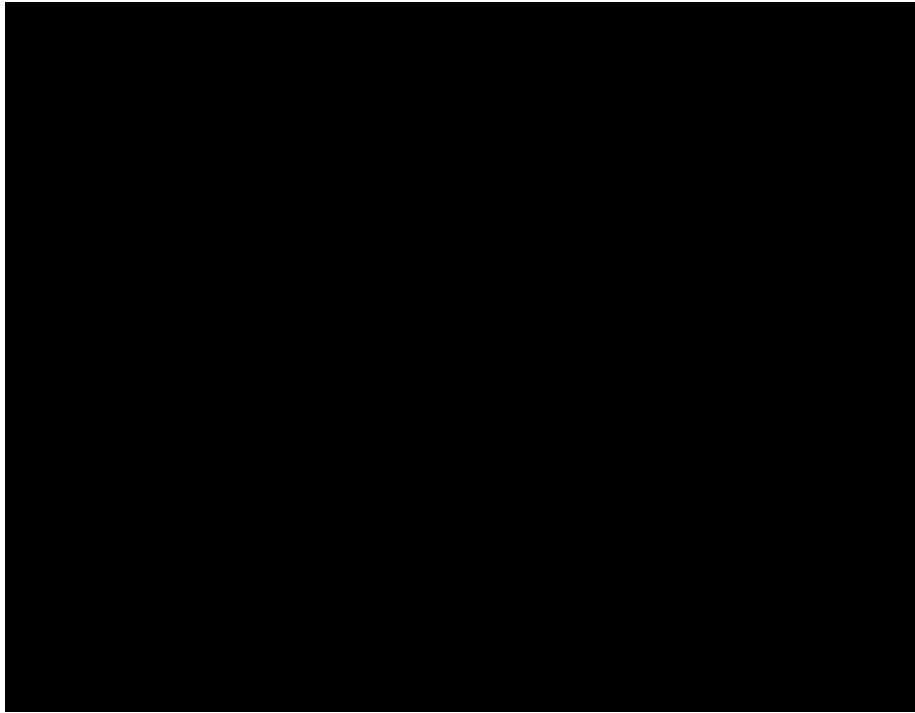


(a) Strake off.

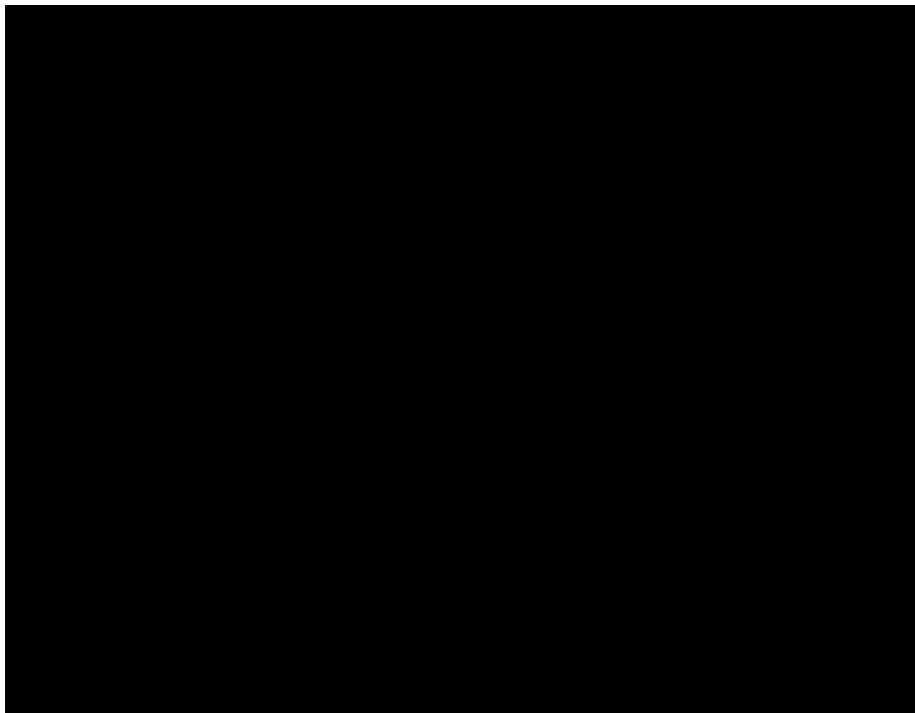


(b) Strake on.

Figure 17. Vapor screen flow visualization at  $M_\infty = 0.80$ ,  $\alpha = 40^\circ$ , and  $\beta = 0^\circ$  with light-sheet position over canopy.

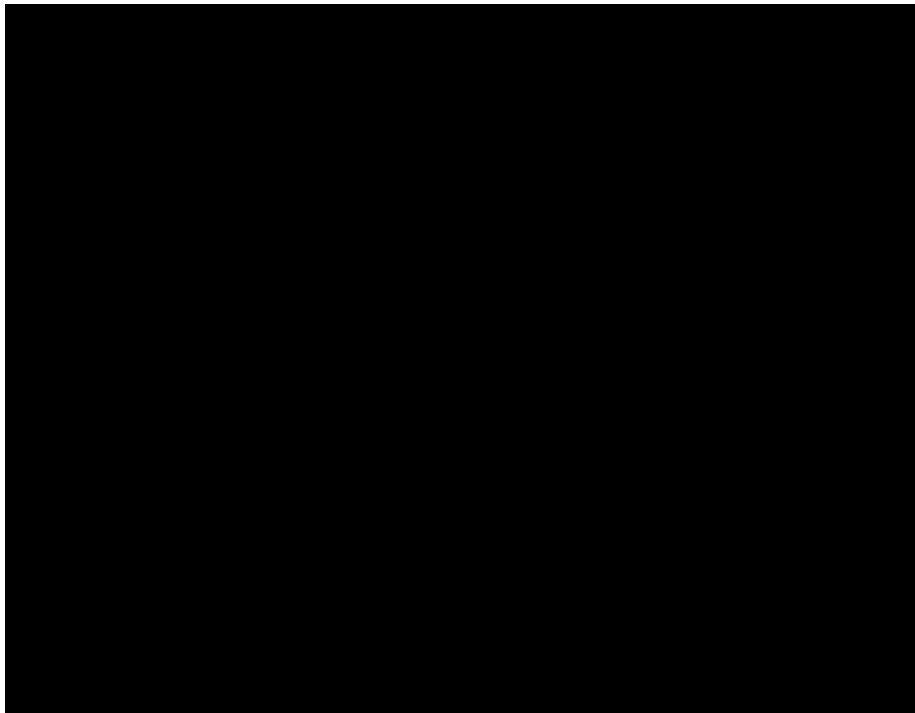


(a) Light sheet over canopy.



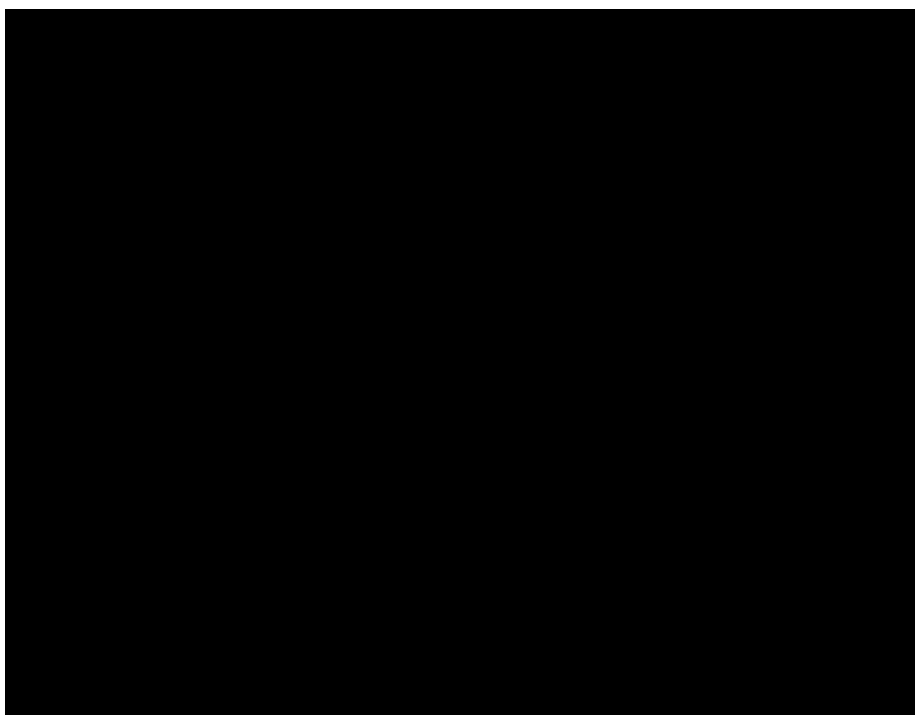
(b) Light sheet downstream of canopy.

Figure 18. Vapor screen flow visualization at  $M_\infty = 0.80$ ,  $\alpha = 40^\circ$ , and  $\beta = 0^\circ$  with baseline strake on.

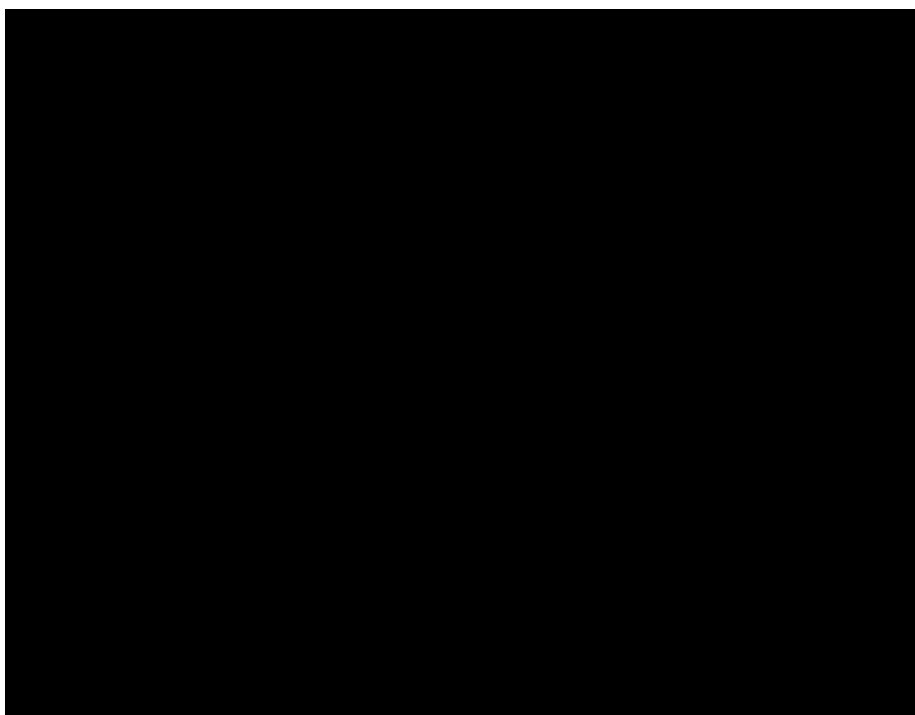


(c) Light sheet near wing mid-chord.

Figure 18. Concluded.

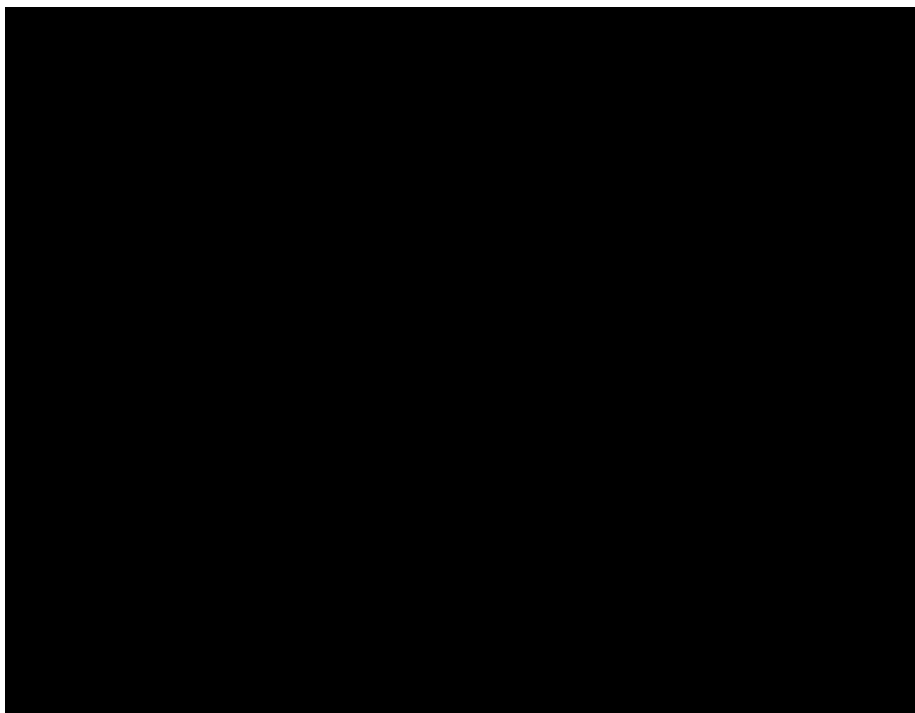


(a)  $\alpha = 40^\circ$ .

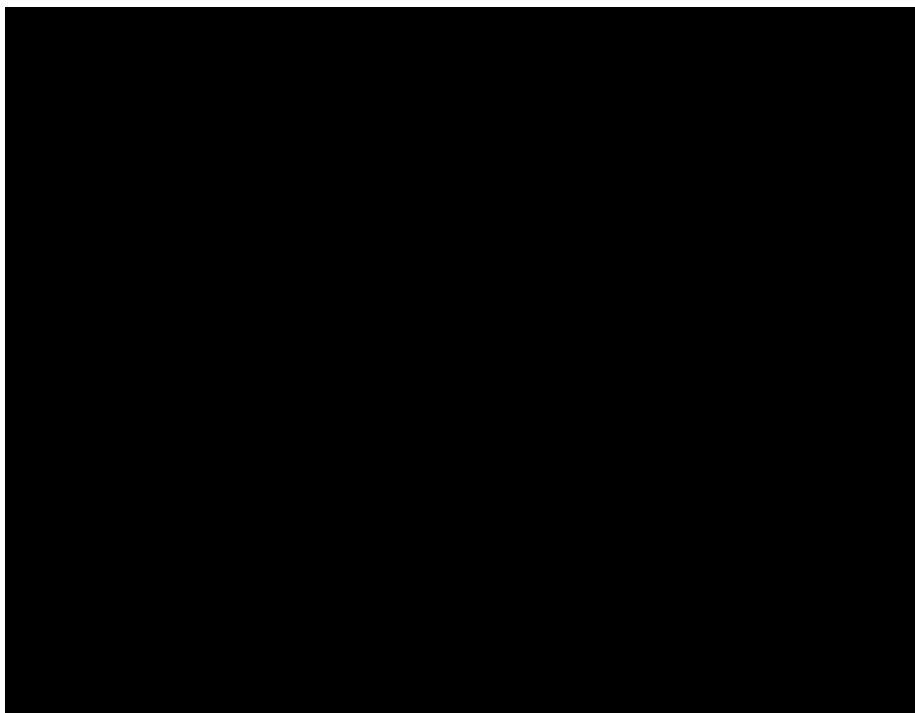


(b)  $\alpha = 50^\circ$ .

Figure 19. Vapor screen flow visualization at  $M_\infty = 0.80$  and  $\beta = 0^\circ$  with baseline strake on and light sheet downstream of canopy.

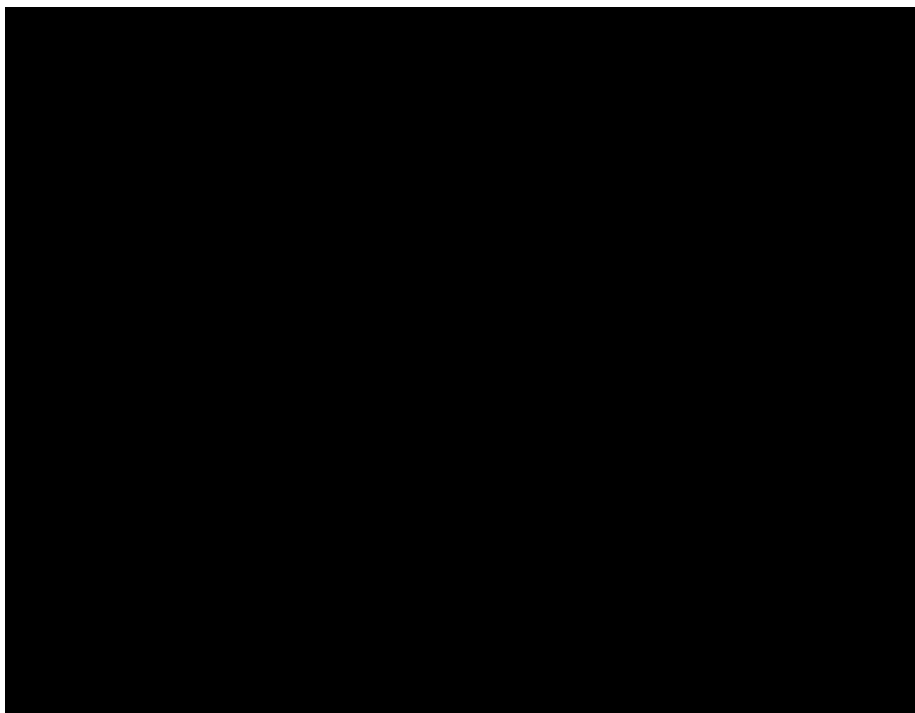


(a)  $\alpha = 50^\circ$ .

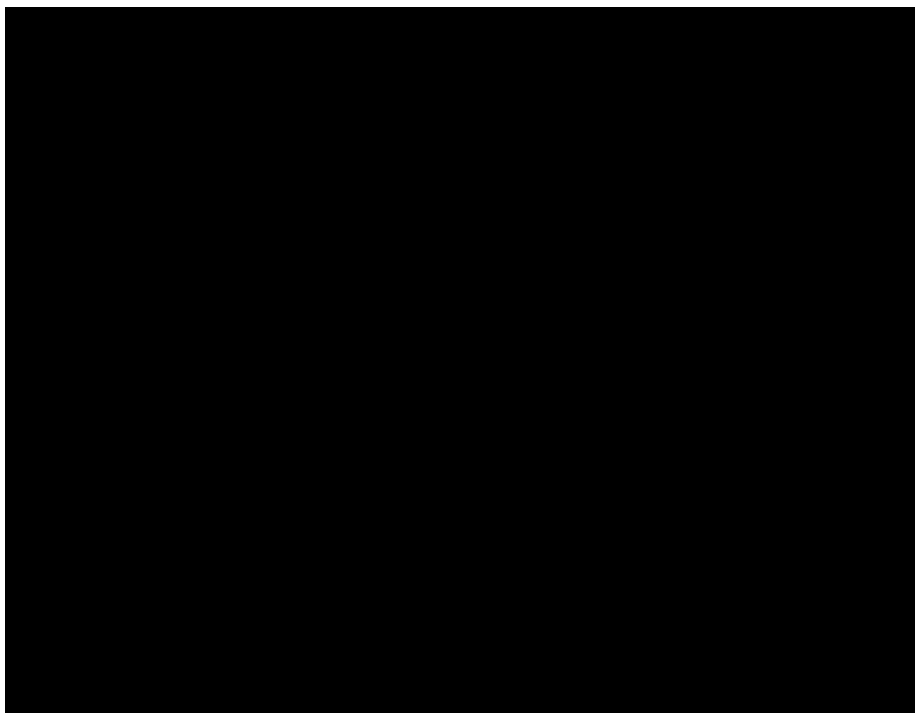


(b)  $\alpha = 55^\circ$ .

Figure 20. Vapor screen flow visualization at  $M_\infty = 0.60$  and  $\beta = 0^\circ$  with baseline strake on and light sheet over canopy.

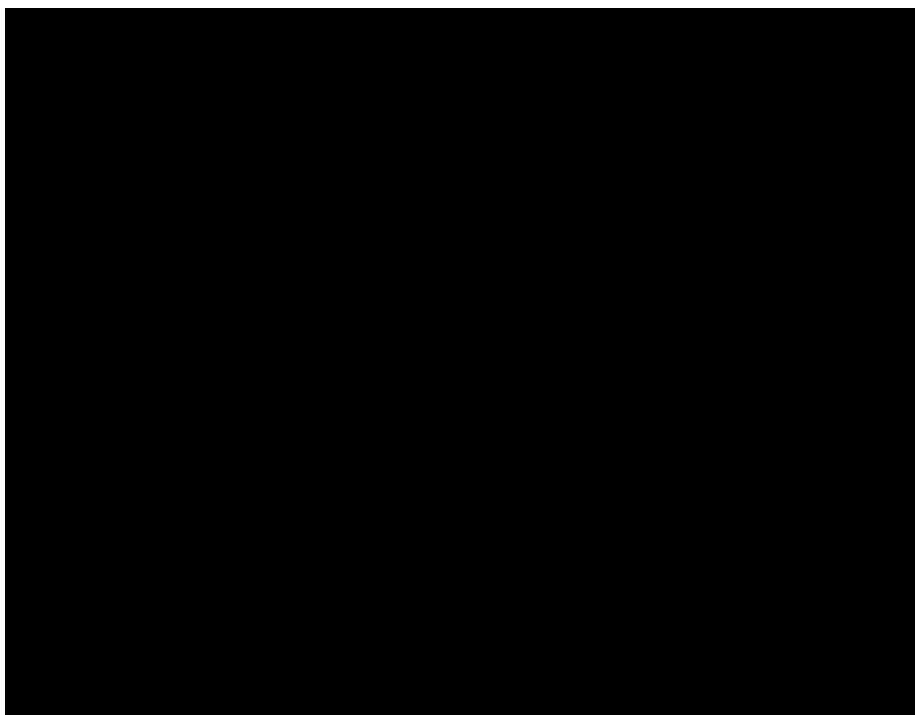


(a)  $\beta = 8^\circ$ .



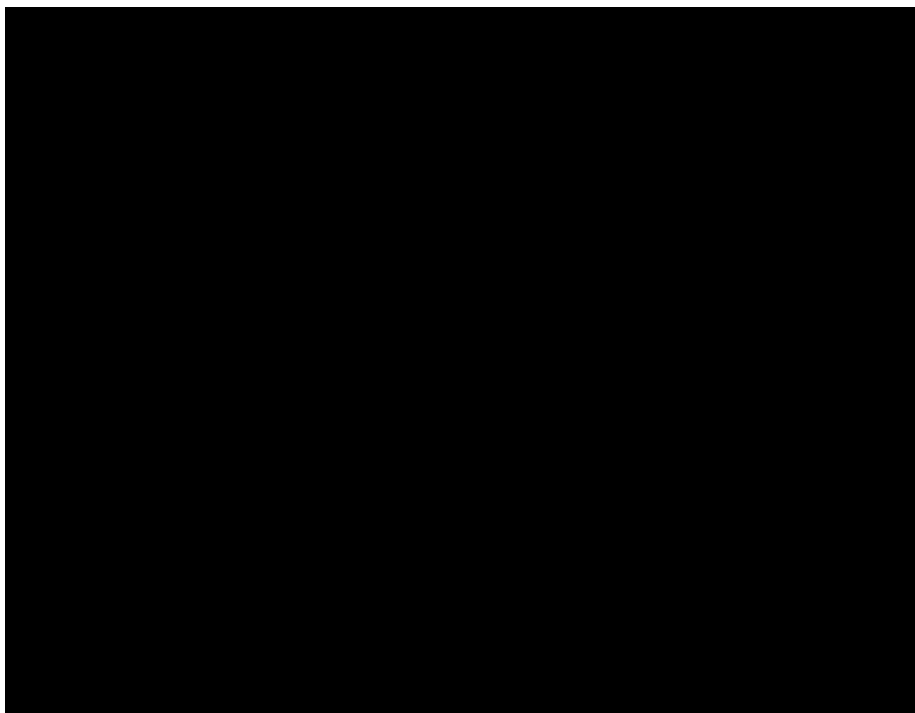
(b)  $\beta = 0^\circ$ .

Figure 21. Vapor screen flow visualization at  $M_\infty = 0.80$  and  $\alpha = 40^\circ$  with baseline strake on and light sheet over canopy.

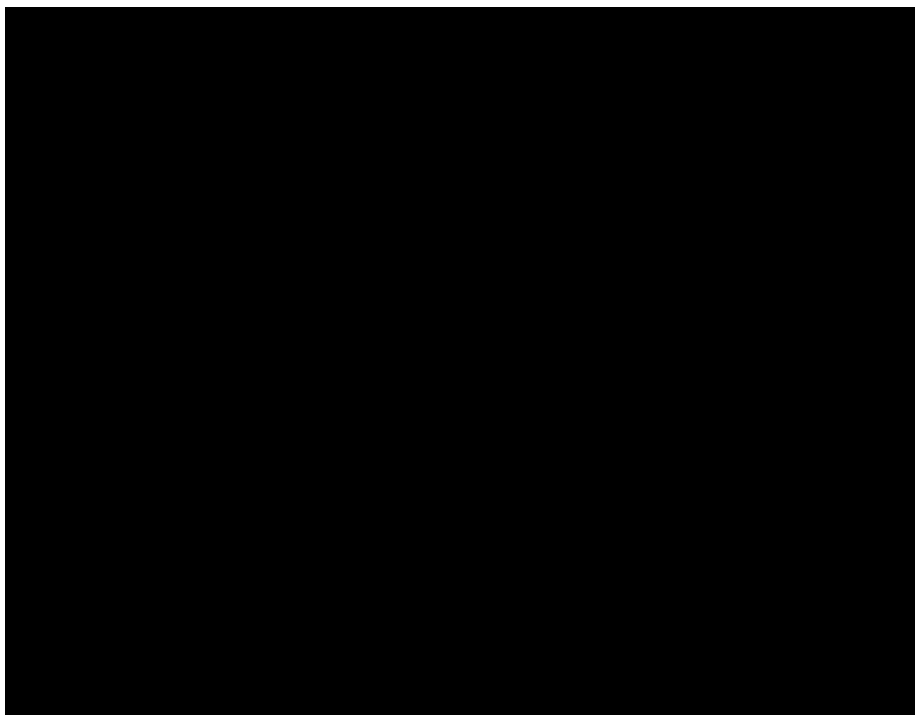


(c)  $\beta = -8^\circ$ .

Figure 21. Concluded.

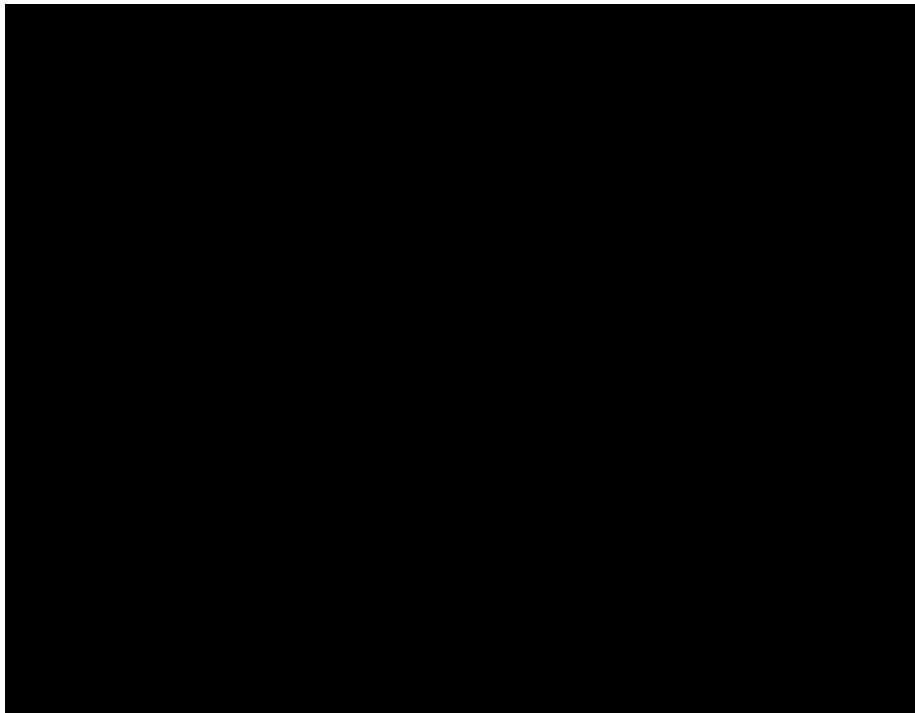


(a)  $\beta = 4^\circ$ .

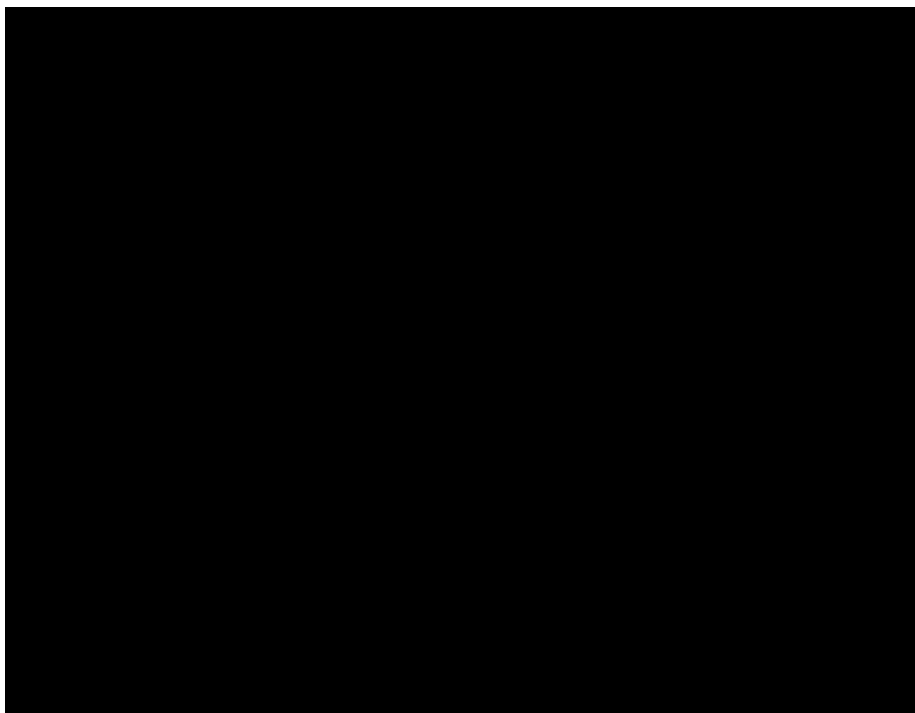


(b)  $\beta = 6^\circ$ .

Figure 22. Vapor screen flow visualization at  $M_\infty = 0.60$  and  $\alpha = 50^\circ$  with baseline strake on and light sheet over canopy.

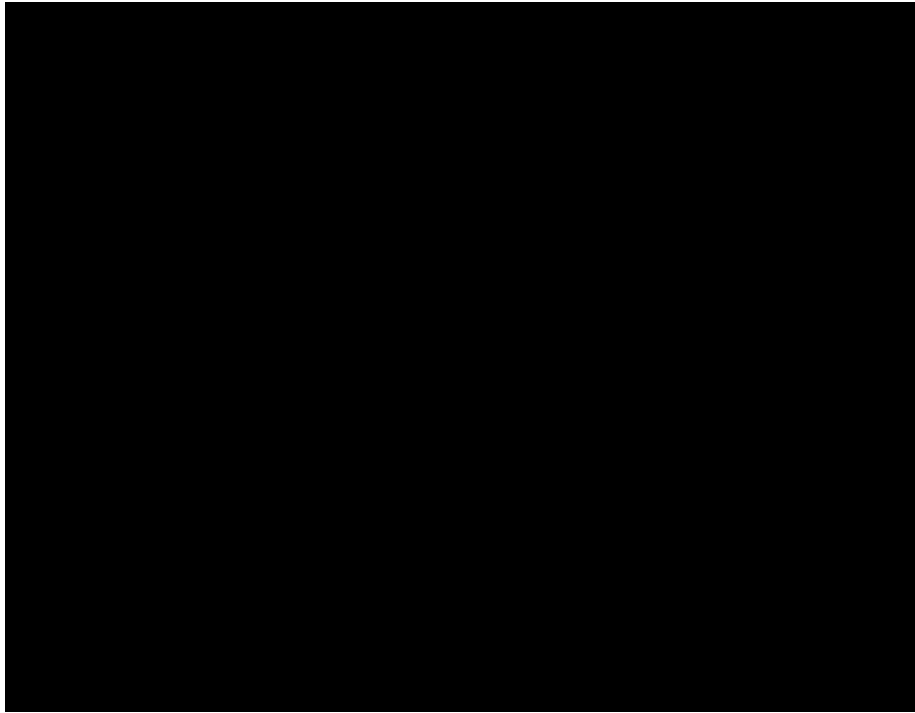


(a) Strake off.

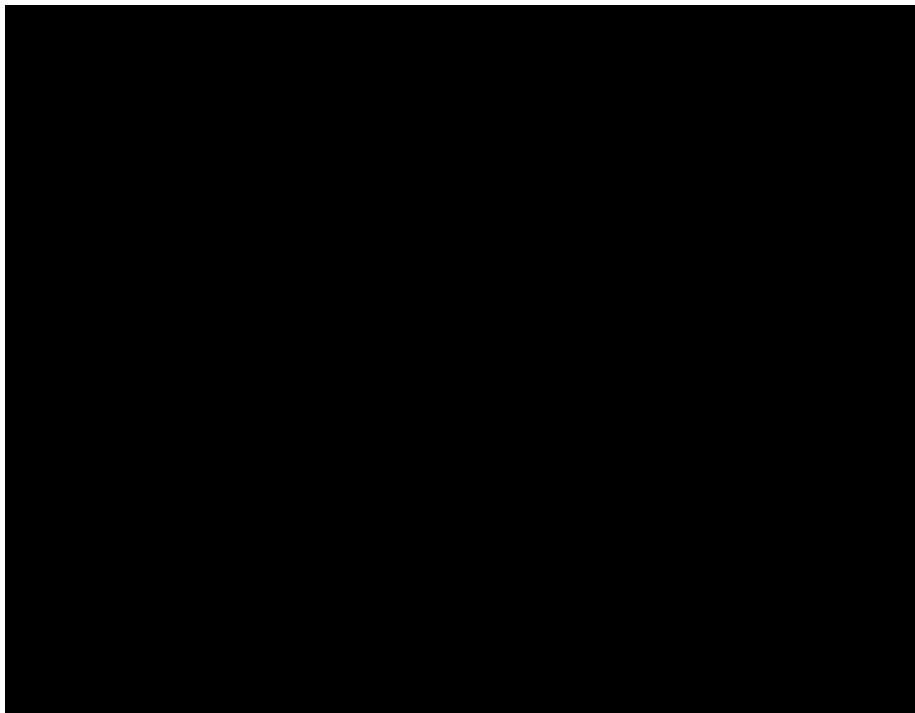


(b) Strake on.

Figure 23. Side view of surface flow visualization at  $M_\infty = 0.40$ ,  $\alpha = 40^\circ$ , and  $\beta = 0^\circ$ .

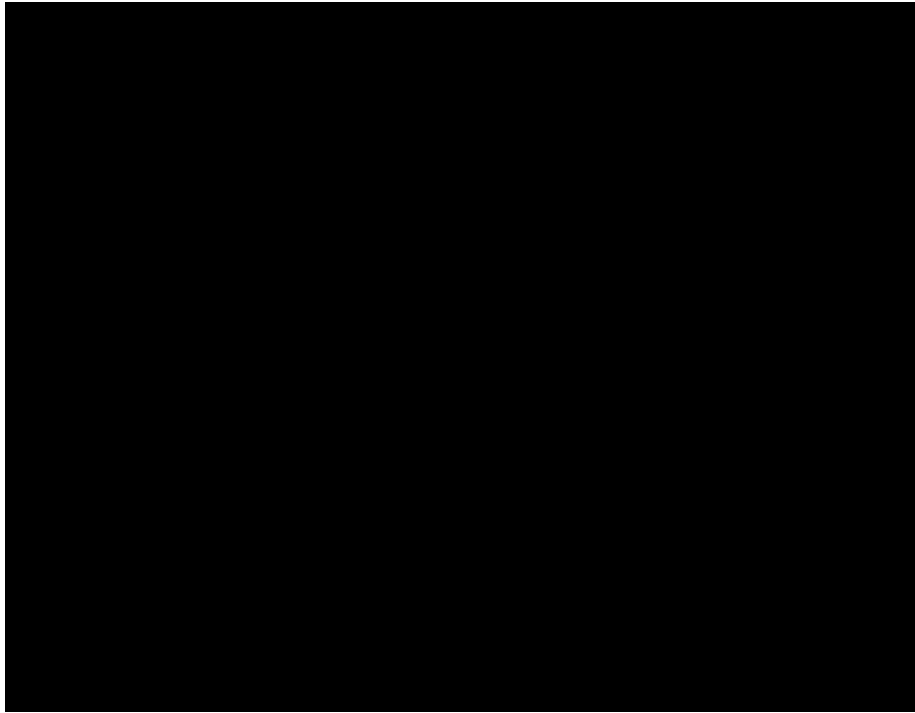


(a) Strake-off side.

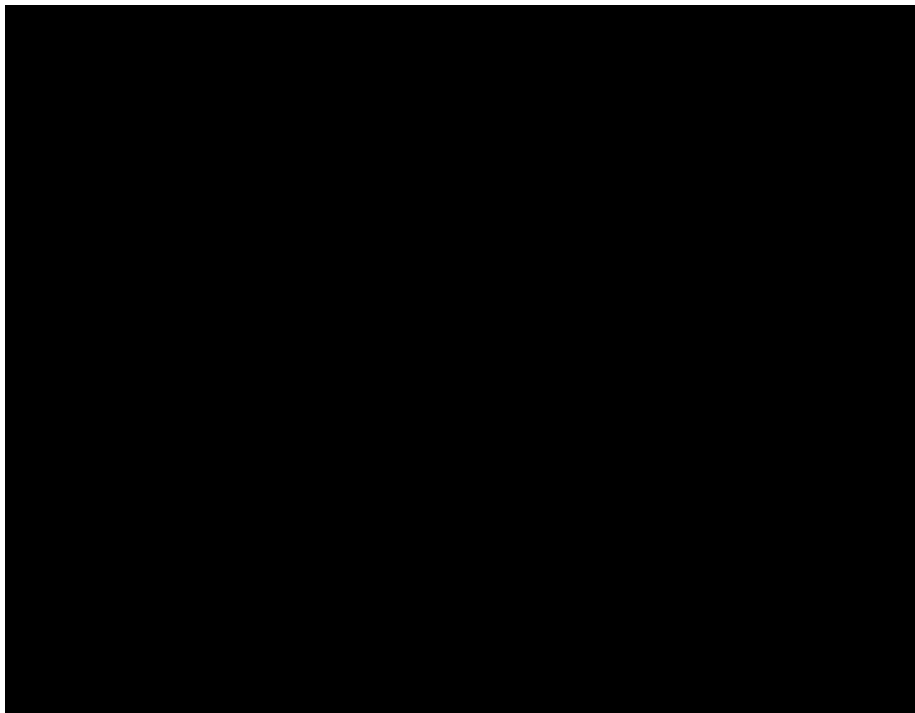


(b) Strake-deployed side.

Figure 24. Plan view of surface flow visualization at  $M_\infty = 0.40$ ,  $\alpha = 40^\circ$ , and  $\beta = 0^\circ$ .



(a) Strake-deployed side.



(b) Strake-off side.

Figure 25. Surface flow visualization at  $M_\infty = 0.40$ ,  $\alpha = 40^\circ$ , and  $\beta = 0^\circ$  with strake on.

Figure 8. The 0.06-scale F/A-18 model in test section of 7- by 10-Foot Transonic Tunnel at DTRC.

L-90-11210

Figure 9. The 0.06-scale F/A-18 forward-fuselage component with aft shroud mounted in Langley 7- by 10-Foot High-Speed Tunnel.

(a)  $\alpha = 20^\circ$ .

(b)  $\alpha = 25^\circ$ .

Figure 10. Vapor screen flow visualization at  $M_\infty = 0.40$  and  $\beta = 0^\circ$  with baseline strake on.

(c)  $\alpha = 25^\circ$  (close-up).

(d)  $\alpha = 30^\circ$ .

Figure 10. Continued.

(e)  $\alpha = 35^\circ$ .

(f)  $\alpha = 40^\circ$ .

Figure 10. Concluded.

(a)  $\alpha = 25^\circ$ .

(b)  $\alpha = 30^\circ$ .

Figure 11. Vapor screen flow visualization at  $M_\infty = 0.40$  and  $\beta = 0^\circ$  with baseline strake on and light sheet near aft canopy region.

(c)  $\alpha = 35^\circ$ .

Figure 11. Concluded.

(a)  $\alpha = 25^\circ$ .

(b)  $\alpha = 30^\circ$ .

Figure 12. Vapor screen flow visualization at  $M_\infty = 0.40$  and  $\beta = 0^\circ$  with baseline strake on and light sheet near LEX-wing junction.

(c)  $\alpha = 35^\circ$ .

Figure 12. Concluded.

(a)  $\alpha = 25^\circ$ .

(b)  $\alpha = 30^\circ$ .

Figure 13. Vapor screen flow visualization at  $M_\infty = 0.40$  and  $\beta = 0^\circ$  with baseline strake on and light sheet near vertical tail apex.

(c)  $\alpha = 35^\circ$ .

Figure 13. Concluded.

(a)  $\alpha = 20^\circ$ .

(b)  $\alpha = 25^\circ$ .

Figure 14. Vapor screen flow visualization at  $M_\infty = 0.80$  and  $\beta = 0^\circ$  with baseline strake on.

(c)  $\alpha = 30^\circ$ .

(d)  $\alpha = 35^\circ$ .

Figure 14. Concluded.

(a) Light sheet near wing mid-chord.

(b) Light sheet near model base.

Figure 15. Vapor screen flow visualization at  $M_\infty = 0.80$ ,  $\alpha = 20^\circ$ , and  $\beta = 0^\circ$  with baseline strake on.

(a) Light sheet near wing mid-chord.

(b) Light sheet near model base.

Figure 16. Vapor screen flow visualization at  $M_\infty = 0.80$ ,  $\alpha = 25^\circ$ , and  $\beta = 0^\circ$  with baseline strake on.

(a) Light sheet near wing mid-chord.

(b) Light sheet near model base.

Figure 17. Vapor screen flow visualization at  $M_\infty = 0.80$ ,  $\alpha = 40^\circ$ , and  $\beta = 0^\circ$  with light-sheet position over canopy.

(a) Light sheet over canopy.

(b) Light sheet downstream of canopy.

Figure 18. Vapor screen flow visualization at  $M_\infty = 0.80$ ,  $\alpha = 40^\circ$ , and  $\beta = 0^\circ$  with baseline strake on.

(c) Light sheet near wing mid-chord.

Figure 18. Concluded.

(a)  $\alpha = 40^\circ$ .

(b)  $\alpha = 50^\circ$ .

Figure 19. Vapor screen flow visualization at  $M_\infty = 0.80$  and  $\beta = 0^\circ$  with baseline strake on and light sheet downstream of canopy.

(a)  $\alpha = 50^\circ$ .

(b)  $\alpha = 55^\circ$ .

Figure 20. Vapor screen flow visualization at  $M_\infty = 0.60$  and  $\beta = 0^\circ$  with baseline strake on and light sheet over canopy.

(a)  $\beta = 8^\circ$ .

(b)  $\beta = 0^\circ$ .

Figure 21. Vapor screen flow visualization at  $M_\infty = 0.80$  and  $\alpha = 40^\circ$  with baseline strake on and light sheet over canopy.

(c)  $\beta = -8^\circ$ .

Figure 21. Concluded.

(a)  $\beta = 4^\circ$ .

(b)  $\beta = 6^\circ$ .

Figure 22. Vapor screen flow visualization at  $M_\infty = 0.60$  and  $\alpha = 50^\circ$  with baseline strake on and light sheet over canopy.

(a) Strake off.

(b) Strake on.

Figure 23. Side view of surface flow visualization at  $M_\infty = 0.40$ ,  $\alpha = 40^\circ$ , and  $\beta = 0^\circ$ .

(a) Strake-off side.

(b) Strake-deployed side.

Figure 24. Plan view of surface flow visualization at  $M_\infty = 0.40$ ,  $\alpha = 40^\circ$ , and  $\beta = 0^\circ$ .

(a) Strake-deployed side.

(b) Strake-off side.

Figure 25. Surface flow visualization at  $M_\infty = 0.40$ ,  $\alpha = 40^\circ$ , and  $\beta = 0^\circ$  with strake on.

(a) Lift.

(b) Pitching moment.

Figure 26. Baseline forebody strake effect on longitudinal aerodynamic characteristics at  $M_\infty = 0.40$  and  $\beta = 0^\circ$ .

(a) Yawing moment.

(b) Side force.

(c) Rolling moment.

Figure 27. Baseline forebody strake effect on lateral-directional characteristics at  $M_\infty = 0.40$  and  $\beta = 0^\circ$ .

(a) Lift.

(b) Pitching moment.

Figure 28. Baseline forebody strake effect on longitudinal aerodynamic characteristics at  $M_\infty = 0.60$  and  $\beta = 0^\circ$ .

(a) Yawing moment.

(b) Side force.

(c) Rolling moment.

Figure 29. Baseline forebody strake effect on lateral-directional characteristics at  $M_\infty = 0.60$  and  $\beta = 0^\circ$ .

(a) Lift.

(b) Pitching moment.

Figure 30. Baseline forebody strake effect on longitudinal aerodynamic characteristics at  $M_\infty = 0.80$  and  $\beta = 0^\circ$ .

(a) Yawing moment.

(b) Side force.

(c) Rolling moment.

Figure 31. Baseline forebody strake effect on lateral-directional characteristics at  $M_\infty = 0.80$  and  $\beta = 0^\circ$ .

(a) Yawing moment.

(b) Side force.

(c) Rolling moment.

Figure 32. Mach number effect on lateral-directional characteristics with baseline forebody strake at  $\beta = 0^\circ$ .

(a) Yawing moment.

(b) Side force.

(c) Rolling moment.

Figure 33. Baseline forebody strake effect on lateral-directional characteristics at  $M_\infty = 0.60$  and  $\alpha = 30^\circ$ .

(a) Yawing moment.

(b) Side force.

(c) Rolling moment.

Figure 34. Baseline forebody strake effect on lateral-directional characteristics at  $M_\infty = 0.60$  and  $\alpha = 40^\circ$ .

(a) Yawing moment.

(b) Side force.

(c) Rolling moment.

Figure 35. Baseline forebody strake effect on lateral-directional characteristics at  $M_\infty = 0.60$  and  $\alpha = 50^\circ$ .

(a) Yawing moment.

(b) Side force.

(c) Rolling moment.

Figure 36. Baseline forebody strake effect on lateral-directional characteristics at  $M_\infty = 0.80$  and  $\alpha = 30^\circ$ .

(a) Yawing moment.

(b) Side force.

(c) Rolling moment.

Figure 37. Baseline forebody strake effect on lateral-directional characteristics at  $M_\infty = 0.80$  and  $\alpha = 40^\circ$ .

(a) FS 107.

(b) FS 142.

(c) FS 184.

Figure 38. Baseline forebody strake effect on forebody surface static pressure distributions at  $M_\infty = 0.40$ ,  $\alpha = 20^\circ$ , and  $\beta = 0^\circ$ .

(a) FS 107.

(b) FS 142.

(c) FS 184.

Figure 39. Baseline forebody strake effect on forebody surface static pressure distributions at  $M_\infty = 0.40$ ,  $\alpha = 30^\circ$ , and  $\beta = 0^\circ$ .

(a) FS 107.

(b) FS 142.

(c) FS 184.

Figure 40. Baseline forebody strake effect on forebody surface static pressure distributions at  $M_\infty = 0.40$ ,  $\alpha = 40^\circ$ , and  $\beta = 0^\circ$ .

(a) FS 107.

(b) FS 142.

(c) FS 184.

Figure 41. Baseline forebody strake effect on forebody surface static pressure distributions at  $M_\infty = 0.40$ ,  $\alpha = 50^\circ$ , and  $\beta = 0^\circ$ .

(a) FS 107.

(b) FS 142.

(c) FS 184.

Figure 42. Baseline forebody strake effect on forebody surface static pressure distributions at  $M_\infty = 0.40$ ,  $\alpha = 55^\circ$ , and  $\beta = 0^\circ$ .

(a) FS 107.

(b) FS 142.

(c) FS 184.

Figure 43. Baseline forebody strake effect on forebody surface static pressure distributions at  $M_\infty = 0.80$ ,  $\alpha = 20^\circ$ , and  $\beta = 0^\circ$ .

(a) FS 107.

(b) FS 142.

(c) FS 184.

Figure 44. Baseline forebody strake effect on forebody surface static pressure distributions at  $M_\infty = 0.80$ ,  $\alpha = 30^\circ$ , and  $\beta = 0^\circ$ .

(a) FS 107.

(b) FS 142.

(c) FS 184.

Figure 45. Baseline forebody strake effect on forebody surface static pressure distributions at  $M_\infty = 0.80$ ,  $\alpha = 40^\circ$ , and  $\beta = 0^\circ$ .

(a) FS 107.

(b) FS 142.

(c) FS 184.

Figure 46. Baseline forebody strake effect on forebody surface static pressure distributions at  $M_\infty = 0.80$ ,  $\alpha = 50^\circ$ , and  $\beta = 0^\circ$ .

(a) FS 107.

(b) FS 142.

(c) FS 184.

Figure 47. Mach number effect on forebody surface static pressure distributions with baseline forebody strake at  $\alpha = 40^\circ$  and  $\beta = 0^\circ$ .

(a) FS 107.

(b) FS 142.

(c) FS 184.

Figure 48. Mach number effect on forebody surface static pressure distributions with baseline forebody strake at  $\alpha = 50^\circ$  and  $\beta = 0^\circ$ .

(a) FS 253.

(b) FS 296.

(c) FS 357.

Figure 49. Baseline forebody strake effect on LEX upper surface static pressure distributions at  $M_\infty = 0.40$ ,  $\alpha = 20^\circ$ , and  $\beta = 0^\circ$ .

(a) FS 253.

(b) FS 296.

(c) FS 357.

Figure 50. Baseline forebody strake effect on LEX upper surface static pressure distributions at  $M_\infty = 0.40$ ,  $\alpha = 25^\circ$ , and  $\beta = 0^\circ$ .

(a) FS 253.

(b) FS 296.

(c) FS 357.

Figure 51. Baseline forebody strake effect on LEX upper surface static pressure distributions at  $M_\infty = 0.40$ ,  $\alpha = 30^\circ$ , and  $\beta = 0^\circ$ .

(a) FS 253.

(b) FS 296.

(c) FS 357.

Figure 52. Baseline forebody strake effect on LEX upper surface static pressure distributions at  $M_\infty = 0.40$ ,  $\alpha = 35^\circ$ , and  $\beta = 0^\circ$ .

(a) FS 253.

(b) FS 296.

(c) FS 357.

Figure 53. Baseline forebody strake effect on LEX upper surface static pressure distributions at  $M_\infty = 0.40$ ,  $\alpha = 40^\circ$ , and  $\beta = 0^\circ$ .

(a) FS 253.

(b) FS 296.

(c) FS 357.

Figure 54. Baseline forebody strake effect on LEX upper surface static pressure distributions at  $M_\infty = 0.40$ ,  $\alpha = 50^\circ$ , and  $\beta = 0^\circ$ .

(a) FS 253.

(b) FS 296.

(c) FS 357.

Figure 55. Baseline forebody strake effect on LEX upper surface static pressure distributions at  $M_\infty = 0.40$ ,  $\alpha = 55^\circ$ , and  $\beta = 0^\circ$ .

(a) FS 253.

(b) FS 296.

(c) FS 357.

Figure 56. Baseline forebody strake effect on LEX upper surface static pressure distributions at  $M_\infty = 0.80$ ,  $\alpha = 20^\circ$ , and  $\beta = 0^\circ$ .

(a) FS 253.

(b) FS 296.

(c) FS 357.

Figure 57. Baseline forebody strake effect on LEX upper surface static pressure distributions at  $M_\infty = 0.80$ ,  $\alpha = 25^\circ$ , and  $\beta = 0^\circ$ .

(a) FS 253.

(b) FS 296.

(c) FS 357.

Figure 58. Baseline forebody strake effect on LEX upper surface static pressure distributions at  $M_\infty = 0.80$ ,  $\alpha = 30^\circ$ , and  $\beta = 0^\circ$ .

(a) FS 253.

(b) FS 296.

(c) FS 357.

Figure 59. Baseline forebody strake effect on LEX upper surface static pressure distributions at  $M_\infty = 0.80$ ,  $\alpha = 35^\circ$ , and  $\beta = 0^\circ$ .

(a) FS 253.

(b) FS 296.

(c) FS 357.

Figure 60. Baseline forebody strake effect on LEX upper surface static pressure distributions at  $M_\infty = 0.80$ ,  $\alpha = 40^\circ$ , and  $\beta = 0^\circ$ .

(a) FS 253.

(b) FS 296.

(c) FS 357.

Figure 61. Baseline forebody strake effect on LEX upper surface static pressure distributions at  $M_\infty = 0.80$ ,  $\alpha = 45^\circ$ , and  $\beta = 0^\circ$ .

(a) FS 253.

(b) FS 296.

(c) FS 357.

Figure 62. Baseline forebody strake effect on LEX upper surface static pressure distributions at  $M_\infty = 0.80$ ,  $\alpha = 50^\circ$ , and  $\beta = 0^\circ$ .

(a) Lift.

(b) Pitching moment.

Figure 63. Strake planform effect on longitudinal aerodynamic characteristics at  $M_\infty = 0.40$  and  $\beta = 0^\circ$ .

(a) Lift.

(b) Pitching moment.

Figure 64. Strake planform effect on longitudinal aerodynamic characteristics at  $M_\infty = 0.60$  and  $\beta = 0^\circ$ .

(a) Lift.

(b) Pitching moment.

Figure 65. Strake planform effect on longitudinal aerodynamic characteristics at  $M_\infty = 0.80$  and  $\beta = 0^\circ$ .

(a) Yawing moment.

(b) Side force.

(c) Rolling moment.

Figure 66. Strake planform effect on lateral-directional characteristics at  $M_\infty = 0.40$  and  $\beta = 0^\circ$ .

(a) Yawing moment.

(b) Side force.

(c) Rolling moment.

Figure 67. Strake planform effect on lateral-directional characteristics at  $M_\infty = 0.60$  and  $\beta = 0^\circ$ .

(a) Yawing moment.

(b) Side force.

(c) Rolling moment.

Figure 68. Strake planform effect on lateral-directional characteristics at  $M_\infty = 0.80$  and  $\beta = 0^\circ$ .

(a) Yawing moment.

(b) Side force.

(c) Rolling moment.

Figure 69. Strake planform effect on lateral-directional characteristics at  $M_\infty = 0.60$  and  $\alpha = 30^\circ$ .

(a) Yawing moment.

(b) Side force.

(c) Rolling moment.

Figure 70. Strake planform effect on lateral-directional characteristics at  $M_\infty = 0.60$  and  $\alpha = 40^\circ$ .

(a) Yawing moment.

(b) Side force.

(c) Rolling moment.

Figure 71. Strake planform effect on lateral-directional characteristics at  $M_\infty = 0.60$  and  $\alpha = 50^\circ$ .

(a) Yawing moment.

(b) Side force.

(c) Rolling moment.

Figure 72. Strake planform effect on lateral-directional characteristics at  $M_\infty = 0.80$  and  $\alpha = 30^\circ$ .

(a) Yawing moment.

(b) Side force.

(c) Rolling moment.

Figure 73. Strake planform effect on lateral-directional characteristics at  $M_\infty = 0.80$  and  $\alpha = 40^\circ$ .

(a) FS 107.

(b) FS 142.

(c) FS 184.

Figure 74. Strake planform effect on forebody surface static pressure distributions at  $M_\infty = 0.40$ ,  $\alpha = 40^\circ$ , and  $\beta = 0^\circ$ .

(a) FS 107.

(b) FS 142.

(c) FS 184.

Figure 75. Strake planform effect on forebody surface static pressure distributions at  $M_\infty = 0.40$ ,  $\alpha = 50^\circ$ , and  $\beta = 0^\circ$ .

(a) FS 107.

(b) FS 142.

(c) FS 184.

Figure 76. Strake planform effect on forebody surface static pressure distributions at  $M_\infty = 0.60$ ,  $\alpha = 40^\circ$ , and  $\beta = 0^\circ$ .

(a) FS 107.

(b) FS 142.

(c) FS 184.

Figure 77. Strake planform effect on forebody surface static pressure distributions at  $M_\infty = 0.60$ ,  $\alpha = 50^\circ$ , and  $\beta = 0^\circ$ .

(a) FS 107.

(b) FS 142.

(c) FS 184.

Figure 78. Strake planform effect on forebody surface static pressure distributions at  $M_\infty = 0.80$ ,  $\alpha = 40^\circ$ , and  $\beta = 0^\circ$ .

(a) FS 107.

(b) FS 142.

(c) FS 184.

Figure 79. Strake planform effect on forebody surface static pressure distributions at  $M_\infty = 0.80$ ,  $\alpha = 50^\circ$ , and  $\beta = 0^\circ$ .

REPORT DOCUMENTATION PAGE			Form Approved OMB No. 0704-0188	
Public reporting burden for this collection of information is estimated to average 1 hour per response, including the time for reviewing instructions, searching existing data sources, gathering and maintaining the data needed, and completing and reviewing the collection of information. Send comments regarding this burden estimate or any other aspect of this collection of information, including suggestions for reducing this burden, to Washington Headquarters Services, Directorate for Information Operations and Reports, 1215 Jefferson Davis Highway, Suite 1204, Arlington, VA 22202-4302, and to the Office of Management and Budget, Paperwork Reduction Project (0704-0188), Washington, DC 20503.				
1. AGENCY USE ONLY (Leave blank)	2. REPORT DATE September 1993	3. REPORT TYPE AND DATES COVERED Technical Paper		
4. TITLE AND SUBTITLE Wind Tunnel Investigations of Forebody Strakes for Yaw Control on F/A-18 Model at Subsonic and Transonic Speeds		5. FUNDING NUMBERS WU 505-68-30-03		
6. AUTHOR(S) Gary E. Erickson and Daniel G. Murri				
7. PERFORMING ORGANIZATION NAME(S) AND ADDRESS(ES) NASA Langley Research Center Hampton, VA 23681-0001		8. PERFORMING ORGANIZATION REPORT NUMBER L-17197		
9. SPONSORING/MONITORING AGENCY NAME(S) AND ADDRESS(ES) National Aeronautics and Space Administration Washington, DC 20546-0001		10. SPONSORING/MONITORING AGENCY REPORT NUMBER NASA TP-3360		
11. SUPPLEMENTARY NOTES				
12a. DISTRIBUTION/AVAILABILITY STATEMENT  Unclassified-Unlimited  Subject Category 02		12b. DISTRIBUTION CODE		
13. ABSTRACT (Maximum 200 words) Wind tunnel investigations have been conducted of forebody strakes for yaw control on 0.06-scale models of the F/A-18 aircraft at free-stream Mach numbers of 0.20 to 0.90. The testing was conducted in the 7- by 10-Foot Transonic Tunnel at the David Taylor Research Center and the Langley 7- by 10-Foot High-Speed Tunnel. The principal objectives of the testing were to determine the effects of the Mach number and the strake planform on the strake yaw control effectiveness and the corresponding strake-vortex-induced flow field. The wind tunnel model configurations simulated an actuated conformal strake deployed for maximum yaw control at high angles of attack. The test data included six-component forces and moments on the complete model, surface static pressure distributions on the forebody and wing leading-edge extensions, and on-surface and off-surface flow visualizations. The results from these studies show that the strake produces large yaw control increments at high angles of attack that exceed the effect of conventional rudders at low angles of attack. The strake yaw control increments diminish with increasing Mach number but continue to exceed the effect of rudder deflection at angles of attack greater than 30°. The character of the strake-vortex-induced flow field is similar at subsonic and transonic speeds. Cropping the strake planform to account for geometric and structural constraints on the F-18 aircraft has a small effect on the yaw control increments at subsonic speeds and no effect at transonic speeds.				
14. SUBJECT TERMS Vortex flows; Subsonic flow; Transonic flow; Flow visualization; Vortex breakdown; Fighter aircraft; Wind tunnels; Lasers; Aerodynamics; Stability; Controllability; Forebody strakes; Forebody controls			15. NUMBER OF PAGES 101	
			16. PRICE CODE A06	
17. SECURITY CLASSIFICATION OF REPORT Unclassified	18. SECURITY CLASSIFICATION OF THIS PAGE Unclassified	19. SECURITY CLASSIFICATION OF ABSTRACT	20. LIMITATION OF ABSTRACT	